

# **Synthesis of Ce & Zr-ZSM-5 Composites and their Electrochemical Studies**



by

*Ali Jawad*

*Registration No.: 00000203322*

A dissertation submitted in partial fulfillment of requirements for the Degree of  
Master of Science in Chemistry

Supervised by

*Dr. Azhar Mehmood*

**School of Natural Sciences (SNS)**


**National University of Sciences and Technology (NUST)**

**H-12, Islamabad 44000, Pakistan**

**June 2021**

**National University of Sciences & Technology****MS THESIS WORK**

We hereby recommend that the dissertation prepared under our supervision by: ALI JAWAD, Regn No. 00000203322 Titled: Synthesis of Ce & Zr-ZSM-5 Composites and Their Electrochemical Studies Be Accepted in partial fulfillment of the requirements for the award of **MS** degree.

**Examination Committee Members**1. Name: DR. MANZAR SOHAILSignature: 2. Name: DR. ASAD MUMTAZSignature: External Examiner: DR. FAROHA LIAQATSignature: Supervisor's Name DR. AZHAR MAHMOODSignature: 
  
 Head of Department

  
 Date
**COUNTERSIGNED**Date: 12/7/2021
  
 Dean/Principal

## **Declaration**

I certify that this research work titled “Synthesis of Ce & Zr-ZSM-5 Composites And Their Electrochemical Studies” is my own work. The work has not been presented elsewhere for assessment. The material that has been used from other sources it has been properly acknowledged / referred.

Signature of Student

Ali Jawad

2019-NUST-MS-Chem-00000203322

## Abstract

Energy generation and storing is a major issue that world is facing nowadays as fossil fuels are running out at a higher pace. So, this is call of time to explore alternative to these conventional energy sources. Scientists have found a number of reusable and natural energy sources other than fossil fuels, which are environment friendly and renewable. Those include solar energy, ocean energy, wind energy etc. but a major problem with the sources is, these do not supply energy uniformly, all the time. So, to maintain a constant source of energy, several storage devices are required, which are able to store energy at peak times of generation and can give away when energy production is low. These storage systems may be in the form of heat storage, mechanical energy storage, batteries or capacitors. Zeolites possess strong catalytic properties due to their highly porous structure and geometry. Along with acting as catalysts, they also carry several other functions for various applications. Hydrothermally synthesized zeolites are used in water treatment, catalytic cracking, organo-chemical conversions and many more. Keeping in view the above mentioned issues, zeolites were opted as a catalyst for water splitting and for capacitive purposes. ZSM-5 was synthesized by solvent free hydrothermal method, along with its two forms doped with 1 gm of Zr and Ce salts. These synthesized ZSM-5 sample and its composites were characterized by XRD, SEM, BET and FTIR techniques, through which ZSM-5 was found to be a highly porous crystalline material, having surface area of 299 m<sup>2</sup>/g. These properties are highly affected by doping. Resultant ZSM-5 and its composites were electrochemically active, so employed as a catalyst for water splitting and for capacitance analysis in pellets form. Zr-ZSM-5 was active towards water splitting, showing current density of 220 mAcm<sup>-1</sup> and taffel slope of 87 mV/dec. Doped samples showed higher dielectric activity as compared to pure one. Ce-ZSM-5 showed dielectric constant of 7.4 x 10<sup>3</sup> with angular losses of 1.5.

## Table of Contents

Synthesis of Ce & Zr-ZSM-5 Composites and their Electrochemical Studies.....	i
Abstract.....	ii
Chapter 1 - Introduction.....	1
1.1 Renewable Energy Sources.....	3
1.2 Energy Storage Technologies .....	4
1.2.1 Mechanical Energy .....	4
1.2.2 Thermal Energy .....	5
1.2.3 Batteries .....	6
1.2.4 Chemical Energy.....	7
1.3 Green Synthesis .....	8
1.4 Electrochemical Properties .....	8
1.4.1 Capacitance .....	8
1.4.2 Static and Time-varying Dielectric Field.....	9
1.4.3 Dielectric Polarization .....	11
1.4.4 Mechanism of Polarization .....	12
1.4.5 Energy Density.....	13
1.5 Water Splitting .....	15
1.5.1 Electrochemistry of Water Splitting Reaction .....	17
1.5.2 Overpotential and Onset Potential .....	18
1.5.3 Tafel Slope and Exchange Current Density .....	18
1.6 Catalysis.....	20
1.7 Zeolites.....	20
1.7.1 Zeolite Synthesis.....	21
1.7.2 ZSM-5 .....	22
1.7.3 Structure of ZSM-5 .....	22
1.7.4 Zeolite doping and its effects .....	22
1.8 Characterization Techniques.....	23
1.8.1 Scanning Electron Microscope (SEM) .....	23
1.8.1.1 Working Principle.....	24
1.8.2 X-Ray Diffraction (XRD) .....	25
1.8.2.1 Working Principle.....	26
1.8.2.2 Instrumentation .....	26

1.8.3 BET- Surface Area Analysis.....	27
1.8.3.1 Working Principle.....	28
1.8.4 Cyclic Voltammetry.....	29
1.8.4.1 Working Principle.....	29
1.8.5 Impedance-Capacitance Analysis .....	29
Aims and Objectives .....	30
Chapter 2 – Literature Review .....	31
Chapter 3 - Materials and Methods.....	37
3.1 Instruments.....	37
3.2 Chemicals.....	37
3.3 Experimental Work.....	38
3.3.1 ZSM-5 Synthesis.....	38
3.3.2 Doping.....	39
3.3.3 Conditions for Characterizations .....	39
3.4 Pellets preparation for impedance capacitance analysis .....	39
3.5 Impedance Capacitance Analysis .....	41
3.6 Electrode Preparation for CV.....	41
3.7 Electrolyte Preparation.....	42
3.8 Electrochemical Operations .....	42
Chapter 4 - Results and Discussion .....	43
4.1 XRD Analysis .....	43
4.2 SEM analysis .....	45
4.3 BET analysis .....	47
4.4 FTIR analysis.....	48
4.5 Impedance Capacitance analysis.....	51
4.5.1 Dielectric Constant study.....	51
4.5.2 Dielectric loss.....	52
4.5.4 Sigma AC.....	53
4.5.6 Complex electric modulus .....	54
4.5.7 Quality factor .....	56
4.6 Water Splitting .....	57
4.6.1 Onset and overpotential .....	57
4.6.2 Tafel slope.....	58

4.6.3 Nyquist plot.....	59
Conclusions.....	61
Chapter 5 - References.....	62

# List of Tables

Table 1: Global power generating capacities of several renewable energy sources

Table 2: List of chemicals

Table 3: Conditions for BET analysis

Table 4: Surface area analysis results

Table 5: Pore volume analysis results

Table 6: Pore size analysis results



# List of Figures

Figure 1: Demonstrating, the increasing trends of CO<sub>2</sub> in atmosphere

Figure 2: Renewable energy sources

Figure 3: Pumped Hydroelectric Storage

Figure 4: Thermal energy storage tank

Figure 5: Different types of battery

Figure 6: Schematic diagram of a parallel plate capacitor

Figure 7: Interaction of electrical field with an atom under classical atomic model

Figure 8: The frequency dependence of the real and imaginary parts of the dielectric constant in the presence of various polarization mechanism

Figure 9: Polarization-electric field responses

Figure 10: Schematic of polarization-electric field response for dielectric material at high field.

Figure 10: Schematic of polarization-electric field response for dielectric material at high field.

Figure 11: Image showing pentasil network of ZSM-5

Figure 12: Illustrative diagram of SEM components

Figure 13: Working of Scanning Electron Microscope

Figure 14: Illustrative diagram of operations of XRD

Figure 15: Instrumental diagram of X-ray Diffraction

Figure 16: Micromeritics BET surface area analyzer

Figure 17: Paste like appearance of materials after grinding

Figure 18: Pallet of pure ZSM-5

Figure 19: Pallet of Zr-ZSM-5 composite

Figure 20: Pallet of Ce-ZSM-5 composite

Figure 21: XRD results of ZSM-5

Figure 22: XRD comparative analysis of three samples

Figure 23: Photograph of synthesized ZSM-5

Figure 24: Photograph of synthesized Zr-ZSM-5

Figure 25: Photograph of synthesized Ce-ZSM-5

Figure 26: FTIR analysis of ZSM-5

Figure 27: FTIR analysis of Zr-ZSM-5 composite

Figure 28: FTIR analysis of Ce-ZSM-5

Figure 29: Plot of  $\epsilon'$  vs  $\ln F$

Figure 30: Plot showing relationship b/w Dielectric loss and  $\ln F$

Figure 31: Plot showing relationship b/w tan loss and  $\ln F$

Figure 32: Plot of relationship b/w sigma AC and  $\ln F$

Figure 33: Complex dielectrics (a) Imaginary part (b) Real part

Figure 34: Cole-cole plots of samples

Figure 35: Plot of Q-factor vs  $\ln F$

Figure 36: Current generation potential vs current density

Figure 37: Tafel slope analysis

Figure 38: Nyquist plots

# Abbreviations and Symbols

AC	Alternating Current
BET	Brunauer-Emett-Teller (Surface area analysis tool)
CV	Cyclic Voltammetry
DPV	Differential Pulse Voltammetry
FTIR	Fourier Transform Infrared Spectroscopy
HEC	Hydrogen Evolution Catalyst
HER	Hydrogen Evolution Reaction
LSV	Linear Sweep Voltammetry
NHE	Normal Hydrogen Electrode
NPV	Normal Pulse Voltammetry
OEC	Oxygen Evolution Catalyst
OER	Oxygen Evolution Reaction
PEM	Proton Exchange Membrane
PNR	Porous Nanorods
RHE	Reversible Hydrogen Electrode
SEM	Scanning Electrons Microscope
SOEC	Solid Oxide Electrolysis Cells
STP	Standard Temperature and Pressure
SWV	Square Wave Voltammetry
TGA	Thermo Gravimetric Analysis
TMP	Transition Metal Phosphides
UN	United Nations
XRD	X-ray Diffraction
ZSM-5	Zeolite Socony Mobil-5

---

---

# Chapter 1 - Introduction

---

---

Global environmental issues are critical international problems and have been snowballing with the rise in world economy. Greatest challenge uprising in the near future of this scientific era which needs to be addressed is the enormous energy requirements. Due to the fact that fossil fuels are running out day by day, as well as the global warming, development of environment friendly and CO<sub>2</sub> emission free fuel is an urgent necessity. Researchers are continuously giving emphasis on their efforts to establish safe, clean and sustainable energy resources to treat out the probable shortage of non-renewable energies and to overcome pollution as well.

“We can no longer burn our way to prosperity,” Ban Ki-Moon, the Secretary General of the United Nations, declared a few years ago. He proposed a well-known challenge to provide universal access to modern energy sources by 2030, quadruple global energy efficiency, and triple global renewable energy consumption. These goals were established as part of a UN project called "Sustainable Energy for All." [1]. Despite the fact that affordable and reliable access to energy has been a key factor for economic and social growth, an estimated 1.3 billion people still do not have access to electricity in a world of approximately 7 billion people.

The world's approximate energy consumption, by year 2012 was about  $5.79 \times 10^{20}$  J, along with a projected energy requirement to target  $8.60 \times 10^{20}$  J by year 2040 [2]. Different estimations are done that how longer the fossil fuel stocks will last. However, it is commonly acknowledged that fossil fuels will not be able to meet the above-mentioned energy demands in the future.

Whenever there is a plentiful supply of energy, there are different challenges to be faced by scientists. According to an estimate, annually about 15 TW energy is being used, of which about 85% is being derived from fossil fuels. Reason behind this excessive usage is their ease of storage, high energy density and transport. It makes natural gas, oil and coal as ideal sources of energy. However, these fuel stocks aren't enough to continue to meet our energy demands forever. Global population is likely to rise up to 9 billion by 2040. As long as population increases, demand for energy also increases, which can rise up to 56% more than it was in 2010 [3]. Even if current rate of consumption doesn't increase, estimated range of reserves is for

about 40-80 years for oil, 150-400 years for coal and 60-160 years for natural gas [4]. The necessity to create viable alternative energy sources is highlighted by declining reserves coupled with uncertain energy security for countries lacking fossil fuel capitals.

Another factor to consider is the impact of greenhouse gas emissions caused by the combustion of fossil fuels with high carbon content. For hundreds of thousands of years, the impact of rising CO<sub>2</sub> concentrations on global mean temperature has been observed, and it is continuing to rise at an unprecedented rate. The globe has changed tremendously since the birth of the industrial revolution, with atmospheric CO<sub>2</sub> concentrations gradually increasing from 280 parts per million to 400 parts per million for the first time in over a month since records began in March 2015 [5]. This concentration will reach 450 ppm in no time if it continues to rise at a rate of roughly 2 ppm per year, posing a major risk of global warming of more than 2oC compared to pre-industrial levels. Such an increase will almost certainly have a severe effect on ecosystems and human culture, [6] To avoid all of this, half of the gas reserves, a third of the oil reserves, and more than 80% of coal reserves should be maintained and not consumed before 2050 [7].

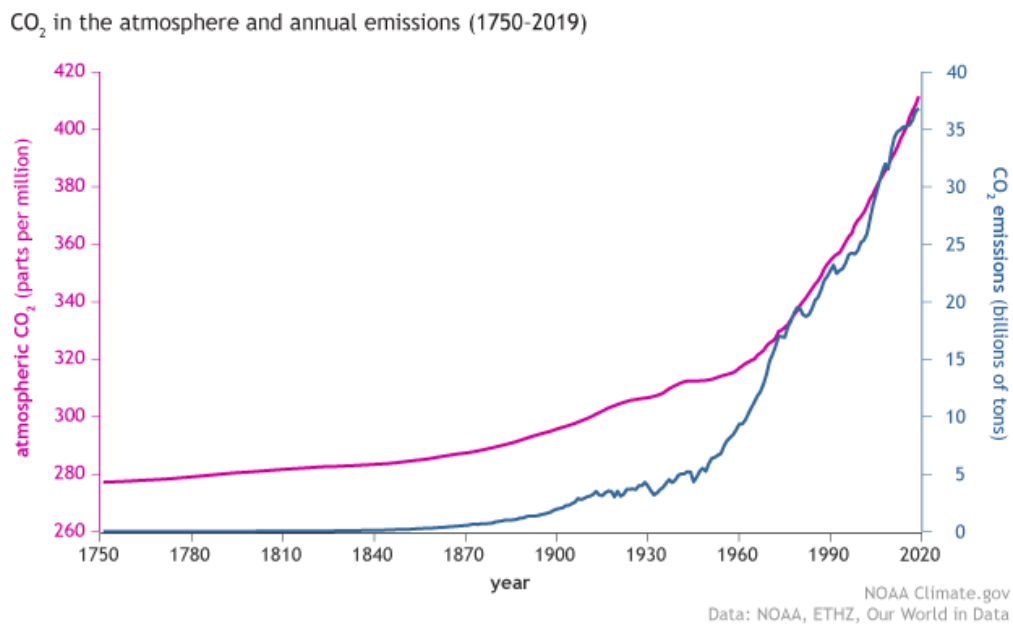


Figure 1: Demonstrating, the increasing trends of CO<sub>2</sub> in atmosphere.

Despite the fact that renewable energy is gaining traction, it is anticipated that we will rely on fossil fuels for more than 75% of our energy by 2040. Renewable energy installations surpassed fossil fuel installations for the first time in 2013, with 143 GW of renewable power sources built vs 141 GW from fossil fuel plants. Government and business are also under pressure from

the public to deploy renewable energy sources and withdraw cash from the coal, gas, and oil industries. Many countries are taking steps to expand renewable energy production while reducing greenhouse gas emissions.

Hydrogen is considered as an ideal fuel in future. Hydrogen as a fuel, can be obtained from renewable and clean energy sources. It is a fuel with no emission of pollutants, when burnt in the presence of oxygen [8]. It is a very promising renewable fuel which can be used in spacecraft's propulsion, in electric devices and aircrafts as well as in vehicles. Hydrogen exists in locked up form in hydrocarbons, water and other organic matter [9]. Scientists are introducing now, different techniques to extract hydrogen from those compounds.

## **1.1 Renewable Energy Sources**

The electricity sector is witnessing a “coming of age” for renewable energy sources. Renewable energy sources provide for up to 13.2% of total primary energy supply and 22% of global electricity generation. By 2040, it is predicted to have increased threefold. There has been a significant rise in investments being done in renewable energy sources, in recent years. Resultantly the share of these sources in energy production has increased in an unusual manner [10]. For an instance, in UK, according to department of Business Energy and Strategy, the contribution of energy in total country's electricity production, by renewable energy sources has increased by 25% between 2014 and 2015[11], and many grants were also given so that new plants can be planted. In Germany, the effects of renewable energy revival can be seen. Germany was a forerunner in adopting renewable energy sources. In 2010, Germany's government unveiled The Energiewende, an ambitious strategy to cut CO<sub>2</sub> emissions by increasing renewable energy output. As a result, renewable energy sources provided almost one-third of the country's electricity in 2015.



Figure 2: Renewable energy sources

## 1.2 Energy Storage Technologies

Generally, there are four technologies used for energy storage purposes, those are: mechanically, thermally, in batteries or in the form of chemical bonds.

### 1.2.1 Mechanical Energy

Mechanical form of energy storage refers to a most ancient method to store energy in bulk, done by mankind. Most common is Pumped Hydroelectric Storage [15]. This method's principle is simple: electrical energy is used to power motors that push water upward from a reservoir at lower level to a higher reservoir, which can be stored as potential form of energy. The water in reservoir is allowed to flow into the lower reservoir to generate electricity, transforming potential energy to kinetic energy, in turn can then be utilized to drive turbines that turn the kinetic energy back into electric current. Unfortunately, this cycle does not correspond to the solar energy diurnal cycle, therefore it does not appear practical to expect to fill and empty a large water tank on a daily basis. Hence, this technique can only be used for long term energy storage purposes.

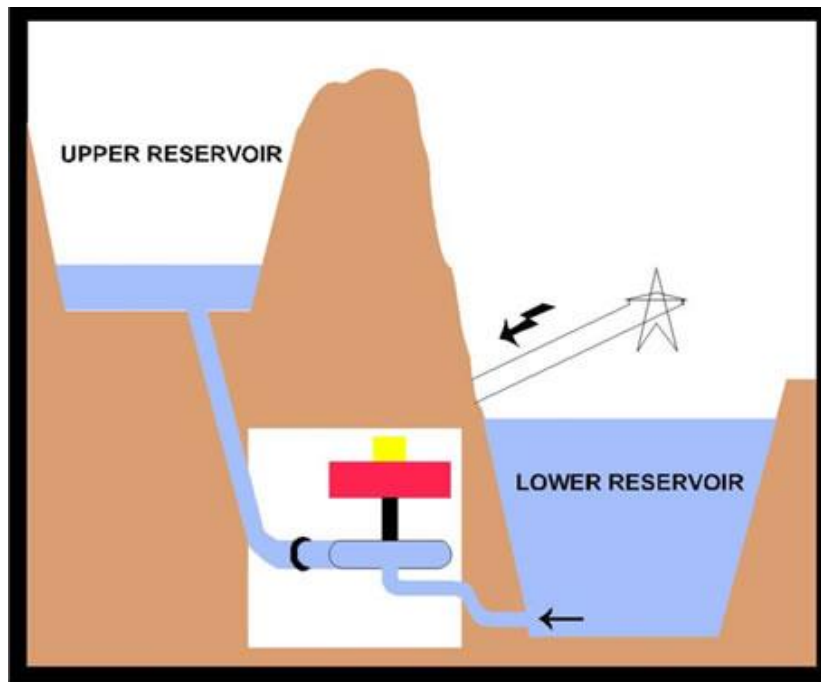


Figure 3: An image of Pumped Hydroelectric Storage

### 1.2.2 Thermal Energy

The second alternative, thermal storage, mostly pertains to Solar Thermal Technology, which heats water or other fluids using sunshine [15]. It can be used to produce hot water and heat for a home on a modest scale, but it may also be applied to large structures and even industry, where heat and vapour are employed in so many operations. This is a relatively simple and practical option that, if properly incorporated into buildings, may significantly reduce fossil fuel consumption, as it has the ability to replace natural gas.



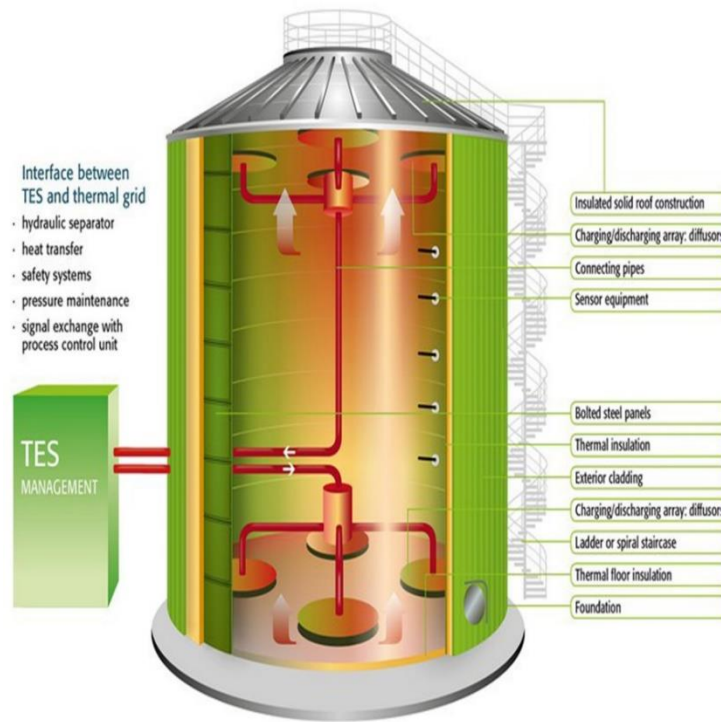


Figure 4: Image showing Thermal energy storage tank

### 1.2.3 Batteries

Batteries are another alternative. Despite the fact that they are common these days, batteries can't be called as the best solution for storage of surplus energy generated by a solar or a wind farm, because of their less energy density, which is defined as the ratio of volume to weight. When it comes to small devices like phones and laptops, low battery energy densities aren't a big concern, but they've proven themselves a stumbling obstacle in larger appliances like electric vehicles. Furthermore, continuous charging and discharging damages the machineries of battery over time, resulting in a constant loss of storage capability and, as a result, less resilience, when joined with high costs of them, makes it nearly unbearable to amortize the costs over the characteristic life span of a photovoltaic system [15].



Figure 5: Images of different types of battery

### 1.2.4 Chemical Energy

Finally, we have chemical bonds as an option of storing energy in them. This involves usage of energy to push an endergonic reaction, with the resultant products being saved and then again reacted to deliver the energy in a controlled way when required. An optimal method used for this purpose is splitting of water into its components. In some ways, plants do the same thing: they split water with sunlight, then join the hydrogen counterparts with CO<sub>2</sub> captured from air to produce carbohydrates. It can be recreated, entire process and storage of energy in the form of methanol, There are a number of options [16], thermolysis includes processes such as water splitting by the use of thermal energy, water cleavage by photobiological method, electrolysis of water, and photo-electrolysis. Thermal water splitting requires materials that can withstand high temperatures as well as a low-cost heat source because water can thermally divided at very high temperatures ranging from 2000 to 2500 °C. This procedure is limited to regions where geothermal energy can be employed because to the need for a cheap heat source. Microorganisms (mostly green algae and cyanobacteria) are used in photobiological water cleavage, and the process is currently too sluggish to be considered. For the time being, electrolysis and photo-electrolysis are the most viable water splitting methods, but maintaining electrolyzer costs low enough to compete with non-renewable energy sources will require a significant amount of work and investment.

### 1.3 Green Synthesis

The branch of chemistry which deals with the synthesis of products in a least pollutants producing pathway, is called as green synthesis.

### 1.4 Electrochemical Properties

Materials with strong electrical resistivities are classified as dielectrics and insulators. Of course, a good dielectric is also a good insulator, but the opposite is not always true. The following are the definitions for dielectric characteristics, dielectric constant, dielectric loss factor, and dielectric strength.

#### 1.4.1 Capacitance

The main feature of a capacitor is that it can store an electrical charge  $Q$ . Following equation gives the charge on a capacitor.

$$Q = CV \quad (1)$$

The applied voltage is  $V$ , and the capacitance is  $C$ . Geometrical and material characteristics are included in the capacitance  $C$ . The geometrical capacitance in vacuum for a large plate capacitor with area  $A$  and thickness  $d$  is provided by the equation below.

$$C_0 = (A/d)\epsilon_0 \quad (2)$$

where  $\epsilon_0$  measures the permittivity of charge storage across vacuum. If a ceramic material of permittivity  $\epsilon'$  is inserted between the capacitor plates,

$$C = C_0 * (\epsilon' / \epsilon_0) = C_0 K \quad (3)$$

The capacitance can be calculated using the equation above, where  $K$  is the relative permittivity or relative dielectric constant. This is a material attribute that determines a circuit element's capacitance[17].

A typical capacitor has a parallel plate configuration, which is made up of two conducting plates separated by an insulating dielectric. An electric field may be generated on the dielectric material when an electrical voltage is applied through two conducting plates. Positive charges are accumulating on one side and negative charges are accumulating on the other. The capacitance, which is used to assess the capacitor's charge storage capacity, is expressed as:

$$C = Q V = \epsilon_0 \epsilon r A / d \quad (4)$$

Where  $Q$  is the cumulative charge on conducting plates,  $V$  is the voltage,  $A$  is the area of conducting plates, and  $d$  is the thickness of the dielectric medium.  $r$  is the relative permittivity, commonly known as the dielectric constant, and  $\epsilon_0$  is the free space permittivity ( $8.85 \times 10^{-12}$  F/m) [18].

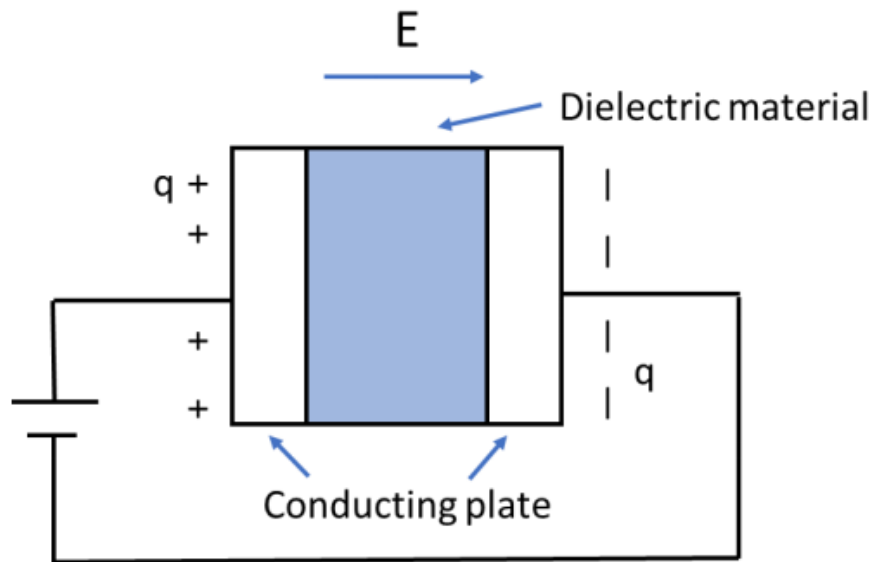


Figure 6: Schematic diagram of a parallel plate capacitor

### 1.4.2 Static and Time-varying Dielectric Field

When an electric field is applied to a dielectric material, it produces electric displacement  $d$ . As a result, we have:

$$d = \epsilon E \quad (5)$$

Where the dielectric constant is a number. The following is the equation for the relationship between relative dielectric permittivity and free space permittivity:

$$\epsilon_r = \epsilon / \epsilon_0 \quad (6)$$

The equation above can be written as:

$$D = \epsilon_0 \epsilon_r E = \epsilon_0 E + P = q_s = (q_s - q_b) + q_b \quad (7)$$

Where  $P$  denotes electric polarization in the presence of an electric field,  $q_s$  denotes surface charge density, and  $q_b$  denotes surface bound charge density.

Polarization can be expressed:

$$P = q_b = \epsilon_o (\epsilon_r - 1)E = \epsilon_o \chi E \quad (8)$$

Where  $\chi$  is defined as electric susceptibility.

Conduction current can also be derived from Maxwell equation:

$$J = \sigma E \quad (9)$$

Where  $\sigma$  is conductivity. Under a voltage with specific frequency, conduction current of dielectric material will change to:

$$JT = J + dD/dt \quad (10)$$

Where J is the conduction current. Time varying electric field with angular frequency  $\omega$  is shown:

$$E = E_m \exp(j\omega t) \quad (11)$$

To get real capacitance for sinusoidal applications and the correct phase shift, a complex permittivity need to be derived:

$$\epsilon^* = \epsilon' - j\epsilon'' = (\epsilon'_r - j\epsilon''_r) \epsilon_o \quad (12)$$

Where  $\epsilon_r'$  is the real part of the permittivity, also called dielectric constant, and  $\epsilon_r''$  is the image part of the permittivity. Dissipation factor (DF), referred to dielectric loss tangent ( $\tan\delta$ ) is used to evaluate the ratio between loss energy to stored energy during charge-discharge cycles.[18]

$$DF = \tan\delta = \epsilon''_r/\epsilon'_r \quad (13)$$

Where  $\delta$  is dielectric loss angel. From physics theory, dielectric loss is the loss energy which transfers to heat due to the rotation of atoms or molecules under alternating electric field.

### 1.4.3 Dielectric Polarization

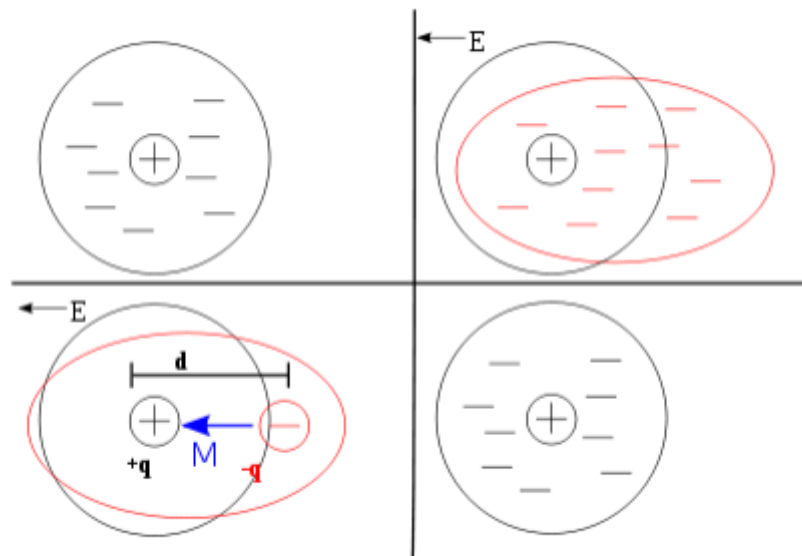


Figure 7: Interaction of electrical field with an atom under classical atomic model

Assume that all substances are made up of atoms. Electron clouds, which are negative charges, and nuclei, which are positive point charges in the centre of the electron clouds, make up atoms. The electron cloud will be distorted (the core of the electron cloud will be shifted) when an electric field is applied, as indicated in the top right of the Fig. 7. Using the superposition principle, this may be simplified to a simple dipole. The dipole moment, represented by the blue arrow labelled  $M$  in Fig. 7, is a vector quantity that characterizes a dipole. The dielectric's behavior is determined by the relationship between the electric field and the dipole moment [19].

The atom will return to its original condition if the electric field is removed. The time required is known as relaxation time (dielectric relaxation), and it is an exponential decrease. In physics, this is the fundamental model. The dielectric's behavior is now determined by the circumstances. In order to effectively capture the behavior, the model must be more complex as the circumstance becomes more difficult [20].

There are two important types of polarization: dipolar polarization and ionic polarization. For the dipolar polarization: The electric field will rotate the covalent bonds (permanent dipoles) (orientation polarization). It can also be produced in molecules when asymmetric nuclei distortion is feasible (distortion polarization). The dipole moment is created by the orientation polarization and distortion polarization. For the ionic polarization: There are positive ions and

negative ions in the ionic crystals (for example, NaCl). When an external electric field is applied, there is a relative displacement between negative ions and positive ions. The centres of the negative charges and positive charges are moved by the electric field. Finally, the dipole moment is formed [21].

#### **1.4.4 Mechanism of Polarization**

Polarization is the process of producing dipoles, which are aligned along the direction of an applied electric field. Polarization is also considered as displacement of charged particles under external an electric field. There are four main types of polarizations:

1. Electronic polarization
2. Ionic polarization
3. Orientational polarization
4. Interfacial polarization [22]

Electronic polarization is the separation of the centers of the electron charges in orbitals and the positive charge in the nucleus, forming dipoles. Ionic polarization is from the change of the distance between neighboring ions in an ionic crystal such as NaCl under electric field [23]. Orientation polarization is due to the alignment of dipoles that can move and rotate freely along the direction of an electric field. Interface Polarization results from the movement of charges happening on the interface such as electrode-material interface.

Interfacial polarization is very small and usually can be neglected. So total polarization  $P$  in dielectric materials can be written as:

$$P = P_e + P_i + P_o \quad (14)$$

Where  $P_e$  is electronic polarization by displacement of electron clouds;  $P_i$  is the ionic polarization by the displacement of ions; and  $P_o$  is orientational polarization by permanent dipole moment [24].

When dielectric materials are under an electric field, dipoles attempt to maintain alignment with the electric field. The time required for this process is different for each polarization mechanism. At lower frequency, dipoles can reorient in time with the electric field. With increasing frequency, dipoles are not able to keep up with the electric field, dielectrics become lossy, and energy is lost in the form of heat. Above the relaxation frequency, the polarization mechanism becomes “frozen” and no longer contributes to total polarization. Figure 1-3 shows

the variation of polarization with frequency for four polarization mechanisms. At optical frequencies, it appears that only electronic polarization is active. Because of the inertia of the molecules and ions, contributions from orientational polarization and ionic polarization are modest at high frequencies. Peaks between 10<sup>12</sup> and 10<sup>16</sup> Hz frequency are caused by resonance effects, in which the electric field alternates at the vibrational frequency of bound ions or electrons, respectively [25].

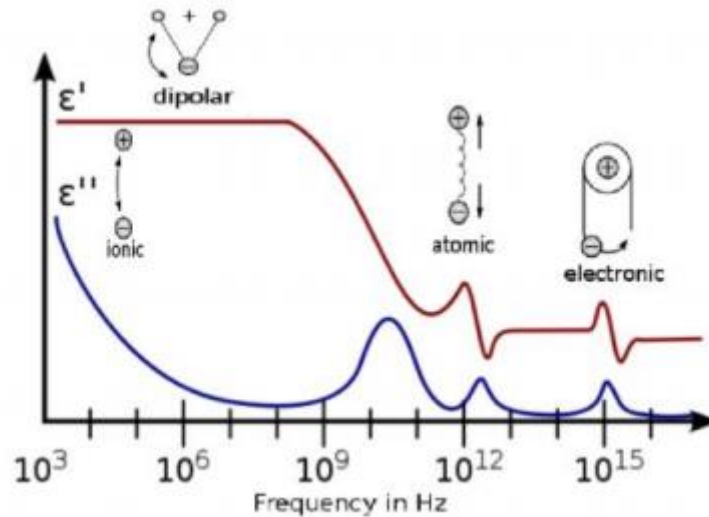


Figure 8: The frequency dependence of the real and imaginary parts of the dielectric constant in the presence of various polarization mechanism.

### 1.4.5 Energy Density

During the charging-discharging process, energy can be stored in the capacitor and then released from it. The energy density  $U_e$  can be express as:

$$U_e = \int E dD \quad (15)$$

In different dielectric materials, the relationship between the polarization and electric field (P-E loop). Energy density is the shaded area in P-E loop[23]. For linear dielectrics, the ratio between the polarization and the electric field is constant. Thus,  $U_e$  can be simplified as:

$$U_e = \epsilon_0 \epsilon_r E^2 / 2 \quad (16)$$



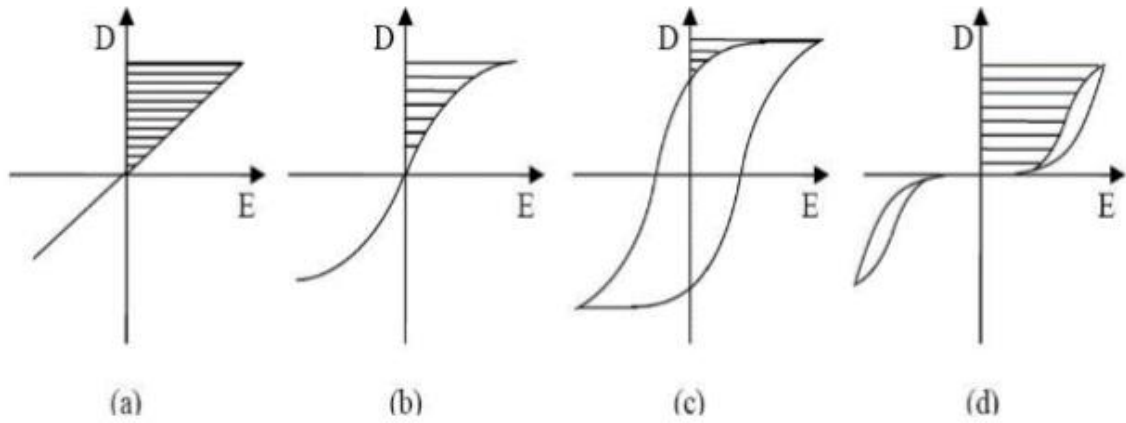


Figure 9: Polarization-electric field responses: (a) Linear (b) relaxor ferroelectric (c) ferroelectric (d) anti-ferroelectric [26]

We can see energy density is proportional to relative dielectric constant  $\epsilon_r$  and the square of electric field. To get high energy density for linear dielectric materials, high dielectric constant and high breakdown strength are needed.

Other dielectrics are non-linear dielectrics, including relaxor ferroelectric, ferroelectric, and anti-ferroelectric materials. Under high electric field, non-linear dielectric materials show a non-linear increase of loss from polarization hysteresis and high field conduction current, especially at high field more than 100 MV/m. The loss under high field is much different from that under low field. To make a comparison, a parameter called energy efficiency ( $\eta$ ) for the charge-discharge cycle is introduced [27].

$$\eta = U_r/U_s = 1 - U_l/U_s \quad (17)$$

where the  $U_s$ ,  $U_r$ ,  $U_l$  are the stored energy density (area I+II), released energy (area I) density and loss density (area II) in the charge-discharge cycle, respectively. The loss under high field can be defined as  $1-\eta$ , which is much higher than that under field below 1 MV/m.

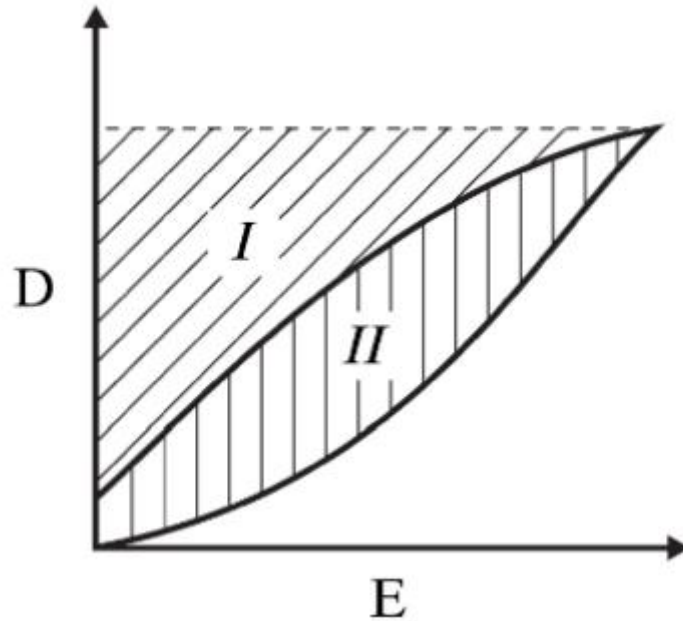
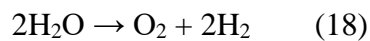


Figure 10: Schematic of polarization-electric field response for dielectric material at high field.

Area **I** shows the charged energy density and **II** corresponds to energy loss density

## 1.5 Water Splitting

The general reaction for water splitting is mentioned as:



It is a thermodynamically ascending procedure that needs  $286 \text{ kJ mol}^{-1}$  of energy contribution under normal conditions of room temperature and pressure. The first water electrolyzers built in the 19th and 20th centuries were initially intended to produce  $\text{H}_2$  for industrial applications, but as a result of the growing need to move away from fossil fuels and toward renewable sources of energy, water splitting has emerged as a promising alternative to fossil fuels [28]. To accomplish so, an electrochemical or photoelectrochemical device is used to split water first. The hydrogen is then kept until it is needed, when it can be burnt in the air or recombined with oxygen in a fuel cell to generate electricity [29].

Splitting of water molecule into its component gases for production of hydrogen is a critical step, for the development of a sustainable greener energy system [30-33]. The whole process of electrochemical water splitting involves two half reactions: first is the Hydrogen Evolution Reaction (HER) taking place at cathode. And the second one is the Oxygen Evolution Reaction

occurring at anode. Since electrolysis of water is not a favorable process thermodynamically. As this reaction takes place at a high overpotential of approximately 1.23V. Therefore, we need several electrocatalysts to enhance the efficiency and kinetics of the reaction. The best catalysts developed so far, for this process are Ir<sub>2</sub>O and Pt metal, which can catalyze OER and HER efficiently at lower overpotentials, respectively [30, 34]. Nevertheless, the cost of material and scarcity of natural source of these noble metals obstruct their application on large scale. Resultantly, more than 90% of hydrogen gas is currently being produced from hydrocarbons source, by steam reforming, which gives out carbon dioxide as a side product. So, the development of efficient catalysts for HER and OER, which are also derivatives of earth abundant elements, is a topic of intense research. There is a number of catalysts, which have been reported recently, a few of which are perovskite oxides, cobalt phosphate and several other transition metal oxides for OER [35-39], and Co-C-N complex [40], nickel molybdenum alloy [41], phosphides and dichalcogenides of transition elements for HER [42-48]. However, practical application of these materials as catalytic electrodes in an integrated electrolyzer is often hindered by the incongruence in electrolytes required when electrodes are coupled, in which both OER and HER result in highest activities and last for a longer period of time.

The two primary types of electrolyzers currently available on the market are proton exchange membrane (PEM) electrolyzers and alkaline-based electrolyzers. The former are the most efficient and capable of achieving current densities [49], alkaline electrolyzers often reach between 100 and 300 mA cm<sup>-2</sup>, but acid electrolyzers typically reach up to 2000 mA cm<sup>-2</sup>. PEM electrolyzers, on the other hand, require very expensive materials since they use valuable metals as electrode catalysts, as opposed to alkaline electrolyzers' catalysts, which are mostly made of Earth-abundant elements. (as for example nickel based spinels and perovskites [50]). Both electrolyzers work at extremely high pH levels, necessitating the usage of materials that can withstand such conditions. Solid oxide electrolysis cells (SOEC) are also under investigation, although they function at extremely high temperatures, necessitating the use of costly materials. When the heat source is taken into account, the efficiency reduces substantially, not to mention the concerns with corrosion, seals, and thermal cycling that must be handled [16].

These electrolyzers are currently in use in some wind and solar farms and run on power generated from any renewable source [51]. From this point forward, we'll concentrate on solar energy because "more energy strikes the globe in one hour ( $4.3 \times 10^{20}$  J) than is spent on the planet in one year ( $4.1 \times 10^{20}$  J)" [15]. In this case, electrolyzers driven by regular solar panels

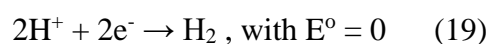
are an indirect method of solar-to-hydrogen generation. A direct approach would be a device in which light harvesting materials coexist with water splitting catalysts, transforming sunlight directly into oxygen and hydrogen. Direct solar-to-fuels devices can be thought of as performing "artificial photosynthesis," capturing and storing sunlight as chemical bonds in a "solar fuel" product [52]. As a result, during the last decade, an increasing number of researchers have focused their efforts on the development of direct solar-to-fuels systems in the hopes of making them more efficient than indirect ones [53, 54]. A direct sunlight to hydrogen device can be configured in two ways from an architectural standpoint. A photovoltaic placed between the water oxidation and hydrogen evolution catalysts performs the light harvesting function in a wireless setup. An electron-hole pair is formed when a photon is received, with the electron going to the Hydrogen Evolution Catalyst (HEC) and the hole going to the Oxygen Evolution Catalyst (OEC). The two electrodes are spatially separated in a wired form, necessitating the use of an external circuit to allow electron passage.

Artificial photosynthesis systems that are both feasible and scalable will need to meet some stringent material specifications. To begin, the current densities that these devices can achieve are limited by the power of incident sunlight, which means that the highest current density that can be achieved is  $30 \text{ mA cm}^{-2}$ , with current densities on the order of  $10 \text{ mA cm}^{-2}$  considered realistic for artificial photosynthesis systems [55]. Electrocatalysts in artificial photosynthesis systems, on the other hand, must be both cheap and versatile [56].

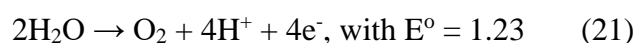
Most known semiconductors suitable for use as light-absorbers degrade rapidly at these pH values, necessitating the use of neutral electrolytes in many artificial photosynthesis applications. Milder pH settings in artificial photosynthesis systems would also help to prevent the degradation of other cell components, which is crucial for long-term performance [57]. Furthermore, pH neutral electrolytes prevent many of the safety concerns that could arise if more caustic electrolytes were used.

### 1.5.1 Electrochemistry of Water Splitting Reaction

A water splitting reaction can be separated into two halves, as shown below:



$$E = E^0 + 0.059 \cdot 2 \log[\text{H}^{+2}] = E^0 + 0.059 \log[\text{H}^+] = 0 - 0.059 \text{ pH} \quad (20)$$



$$E = E^o + 0.059 \cdot 4 \log H^{+4} = E^o + 0.059 \log H^+ = 1.23 - 0.059 \text{pH} \quad (22)$$

According to the preceding equations, in principle, a voltage difference of 1.23 V between the anode and the cathode is all that is required to split water, but in fact, due to cell resistances and the requirement to overcome kinetic barriers at each electrode, a higher potential is required [63]. The overpotential  $\eta$  is the difference between the real potential we require to split water and the theoretical potential, and the voltage we need to apply becomes:

$$E_{\text{applied}} = 1.23 + \eta_{\text{anode}} + \eta_{\text{cathode}} + iR \quad (23)$$

The resistance loss can be reduced by improving the cell design, and we add catalysts to each electrode to deal with the activation barriers, with the goal of lowering the overpotential as much as possible to reduce the energy input required to drive the reaction [64].

While the pH terms cancel each other out in the overall equation and so don't matter in an electrolyzer, they do matter when we use a potentiostat to evaluate the performance of a catalyst for one of the two half-reactions [65]. The formula used to convert ERHE to and from ENHE is given as:

$$ERHE = ENHE + 0.059 \times \text{pH}. \quad (24)$$

For example, if we want to apply a potential of 1 V vs RHE, this will be 1.41 V vs NHE at pH 7 and 1.83 V at pH 14[66].

### 1.5.2 Overpotential and Onset Potential

We use the overpotential necessary to generate a certain current density, which is commonly 10 mA cm<sup>-2</sup> for HECs and 1 mA cm<sup>-2</sup> for OECs, to compare different catalysts [66]. Many researchers also discuss "onset overpotential," which is the point at which activity for the half-reaction under study begins to manifest, although this word isn't very useful unless it's used in conjunction with a current density number, because there's no clear definition of "onset." [67].

### 1.5.3 Tafel Slope and Exchange Current Density

The Tafel slope is most likely the measure that best reflects an electrocatalyst's performance. Before discussing the significance and utility of the equation, we'll go through where it came from.

In the absence of mass transport constraints, the steady state current density is thought to follow the equation:

$$j = j_0 e^{\alpha F \eta / RT} \quad (25)$$

where  $j_0$  is the exchange current density,  $\alpha$  represents the transfer coefficient,  $\eta$  is the overpotential.

If we take natural logarithms the equation becomes

$$\ln j = \ln j_0 + \alpha F \eta / RT \quad (26)$$

and if we convert it to natural logarithms

$$2.303 \log j = 2.302 \log j_0 + 2.303 \alpha F \eta / RT \quad (27)$$

And dividing by 2.303

$$\log j = \log j_0 + \alpha F \eta / 2.303 RT \quad (28)$$

Which can be arranged as

$$\eta = a + b \log j \quad (29)$$

The Tafel equation is an expression in which  $a$  and  $b$  are constants. If we record the steady state current density given by our catalyst at various potentials and plot it as logarithm of the current density vs the overpotential, we should be able to find a linear region that satisfies this equation. Because we are using logarithms and the slope is stated in units of  $\text{mV dec}^{-1}$ , we can see the overpotential increment required to increase the current density by an order of magnitude, say from 1 to 10  $\text{mA cm}^{-2}$ , at a glance. Lesser the Tafel slope, better is the catalyst, because it means that bigger increments of overpotential are required to achieve higher current densities, and that we can "tune" the current density with minor changes in overpotential. We must remember that with an electrolyzer, we are unlikely to want a fixed current density, therefore a catalyst that can operate over a wide range of current densities with little change in the overpotential is highly desirable [49].

Although the Tafel slope equation is commonly recognized and can be used to almost any heterogeneous electrocatalyst, it was designed for metallic electrodes, hence its applicability to electrodes that aren't wholly metals should be handled with caution. Whereas talking about electron concentration in a metal makes no sense [68].

## 1.6 Catalysis

Catalysis is the most important application of zeolites. The importance of zeolites in catalysis makes their way from the fact that they possess various structural characteristics. Zeolites are ranked amongst the most porous material with a large internal surface area and a low framework density. Some key features of zeolites include pores defined substrate size, catalytic cracking, specified sized filtration, removal of hardness of water and in other organo-chemical conversions. These are porous solids, possessing a huge number of active sites as compared to other solid catalysts.

## 1.7 Zeolites

Zeolite which is a huge class of minerals containing hydrated aluminosilicates of sodium, potassium, calcium, and barium or can be easily rehydrated and dehydrated, also used as cation exchanger and molecular sieves is broadly used for the sake of heterogeneous catalysts in oil refining and petrochemical industry by means of solid acid catalysts [69]. Though, it contains some limitations by means of diffusional perspectives which carry many complications like reduction in reaction rate and deactivation [70]. Diffusion length reduction in the zeolite crystals can lighten molecular transport problems as well. Yet, its production is not always easy. So, in order to create a supplementary array in zeolites, its molecular sieves fabrication with mono-crystalline hollow structures appeals extensive consideration [71],[72]. Presently, there are many reports whose main focus is dependent on MFI molecular sieves [73], because of its exceptional pore channel structure, its thermal stability and thus have huge potential in many catalytic reactions unlike the hollow, single crystal ZSM-5 zeolite molecular sieves which contain limited reports about it [74].

Zeolites are no longer minerals that have only been exhibited in museums and since their wide use in processing have become a commercial and science success story. It all started with the use, both for oil and petrochemicals, of synthetic zeolites. The foregoing now is part of the history of the industry: a case study of innovation and development and a model for engineering and technology interpositions. In particular, Marcilly's two-volume contribution is a mandatory reading for the deep and broad coverage of the serious beginner; furthermore, a knowledgeable practitioner who knows the basic and the applied aspects of zeolite as well as other acid-base catalytic processes offers a unique perspective. Geological discovery and industrial interest to efficient, large-scale zeolite processing and use in catalytic or adsorption processes. This model shows a strong partnership between science and technology [75].

Zeolite or zeolite-like materials are porous crystalline three-dimensional framework based essentially on tetrahedrally coordinated T-atoms characterized by the presence of channels (and eventually cages) with the smallest opening larger than six T-atoms (where T = Si, Ge, Ti, Al, Ga, B, Fe, Be, P, etc.). The T-atoms forming the framework are linked together by the common sharing of oxygen ions to form poly-nuclear complexes. Different types of zeolites result from differences in the way how the T-atoms may link in the space. The tri-dimensional networks encompass well defined micropores with uniform pore diameters that are similar to the dimensions of simple organic molecules. Pore diameters depend on the number of T-atoms in the ring around the pore. According to the number of T-atoms forming the pore opening zeolites, are grouped as follows: [76].

1. Small-pore zeolites (8- membered rings), e.g., Erionite
2. Medium-pore zeolites (10-membered rings), e.g., ZSM-5, ZSM-11, ferrierite, MCM-22
3. Large-pore zeolites (12-membered rings), e.g. zeolite Y, Beta, mordenite, ZSM-12
4. Extra-large-pore zeolites (14-membered rings), e.g. CIT-5 and UTD-1.

### **1.7.1 Zeolite Synthesis**

Zeolites are known to consist of micro aluminosilicate crystals used as ion substitutes for the detergent industry, radioactive waste treatment, processing of liquid waste, separators for purifying water and catalytic oil cracking and petrochemical industries. All these functions are characterized by the uniform pores in their size and form, mobility and hydrophobic nature to some solutes in several industries [77]. In some cases, they can perform these functions in several industrial applications. Primarily, zeolites are built from  $\text{SiO}(\text{AlO}_4)\text{-5-Tetrahedral}$  extended infinitely over a 3-D network, connected by a common oxygen atom. The  $\text{TO}_4$  can be represented as the main building block, with either T-silicon (Silicon-Aluminum ( $\text{Al}^{3+}$ )) ions, whereas the  $\text{O}_4$  represents each of the oxygen atoms, which is distributed by both T-atoms. The T-silicon (Al, Se,  $\text{Al}^{3+}$ ) ions are also included. Zeolite may be defined as the material consisting of micro porous, detergent ion exchangers, radioactive storage, liquid waste, cleansing, disinfectants and environmental controls, petrochemical, biomass, refined chemicals, drying and processing separators [78]. All these functions can be owing to their linity and hydrophilic and/or hydrophobic nature as a catalyst in several industrial applications. Zeolites are constructed primarily by one silicon and four oxygen comprising tetrahedral molecule ( $\text{SiO}_4$ ), extending infinitely over three dimensions with a common tetrahedral oxygen, frequently known as the primary building block, which also represents a silicone ( $\text{-SiO}_4\text{-}$ ).



Zeolites are represented by the general definition of an alkaline metal cation,  $b$  is a valence of an alkaline or an alkaline earth metal cation and  $b$  is the volume per unit cell of the zeolite of crystal-like gas, and  $y$  is the complete tetrahedral count in the unit cell,  $c$  is the quantity by cell of a cation of the earth of alkali or alkali of the earth, But in the case of a silica-based zeolite,  $y/a$  can actually exist for more than 200 forms and the atomic composition of zeolites can have aluminium (Si / Al) ratios. The ratio varies from 1 in silicon, which is a modified zeolite of aluminium free crystalline silica.

### 1.7.2 ZSM-5

Zeolite Socony Mobil 5 is an aluminosilicate zeolite, possessing pentasil framework, which belongs to pentasil zeolite family. Its general and chemical formula is  $\text{Na}_n\text{Al}_n\text{Si}_{96-n}\text{O}_{192} \cdot 16\text{H}_2\text{O}$  ( $0 < n < 27$ ). It was patented in 1975 by a Mobil Oil company. This material is widely used as a heterogeneous catalyst in Petrochemical industries for hydrocarbons isomerization reactions.

### 1.7.3 Structure of ZSM-5

This zeolite is composed of several pentasil ring shaped units, which are linked together through oxygen bonds also known as bridges. One pentasil unit comprises of eight five-membered rings. In these rings, Si and Al are thought to be located at vertices, and O atoms are supposed to be bonded between the vertices.

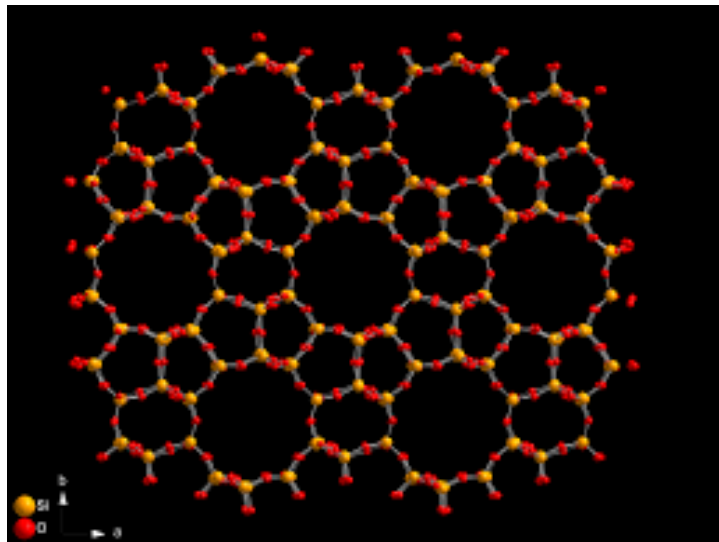


Figure 11: Image showing pentasil network of ZSM-5

### 1.7.4 Zeolite doping and its effects

Natural zeolites are one of these materials which are most promising to remove ethylene [79]. Zeolites act as molecular sieves in purification processes due to their large area and cation

exchange ability. Other properties, like their non-toxicity, abundance, economic and environmental acceptable properties, make zeolites an exceptional sorbent material for agri-business. The surface is charged to the negative degree by replacing silicon with aluminum atoms in a zeolite structure, which is required to carry the deficiency of the Lewis acid or of the heavy Bronzed acid sites by means of further metal cations or hydexylprotoms. The potential of intermediate divalent metal to be substituted for cations increases zeolite adsorption and catalytic properties.

Divalent cations have a lower ionic radius than monovalent cations and are enabled to improve access to adsorption sites for ethylene. Zeolites with divalent counter-cations such as  $\text{Cu}^{2+}$  and  $\text{Zn}^{2+}$  exhibit favorable ethylene adsorptions because of the interaction among the two-loaded cations with the quadruple moment of ethylene. The first reaction between strongly electronegative oxygen on the natural zeolite surface and hydrogen of the C-H bond of ethylene is prior to the weak H-bonding interactions [80].

## **1.8 Characterization Techniques**

Several analytical and characterization techniques are utilized to analyze the subject materials. The results obtained from these techniques give us information about the physical and chemical properties of material. These include chromatography, spectroscopy, electrochemical and gravimetric analysis etc. Several characterization techniques were utilized for confirmation of material formation and then for activities testing. Introduction of these techniques is as:

### **1.8.1 Scanning Electron Microscope (SEM)**

It is a technique using highly energetic electron source. In SEM high energy electrons give us info about the external morphology, crystallinity and general chemistry of the sample, ranging from nano-scale to micro-meter. Results are displayed in the form of images. Along with being a non-destructive technique, SEM also provides the facility of analysis over a specified area of sample and generates images in a two-dimensional format. Different components of scanning electron microscope instrument are shown in figure:

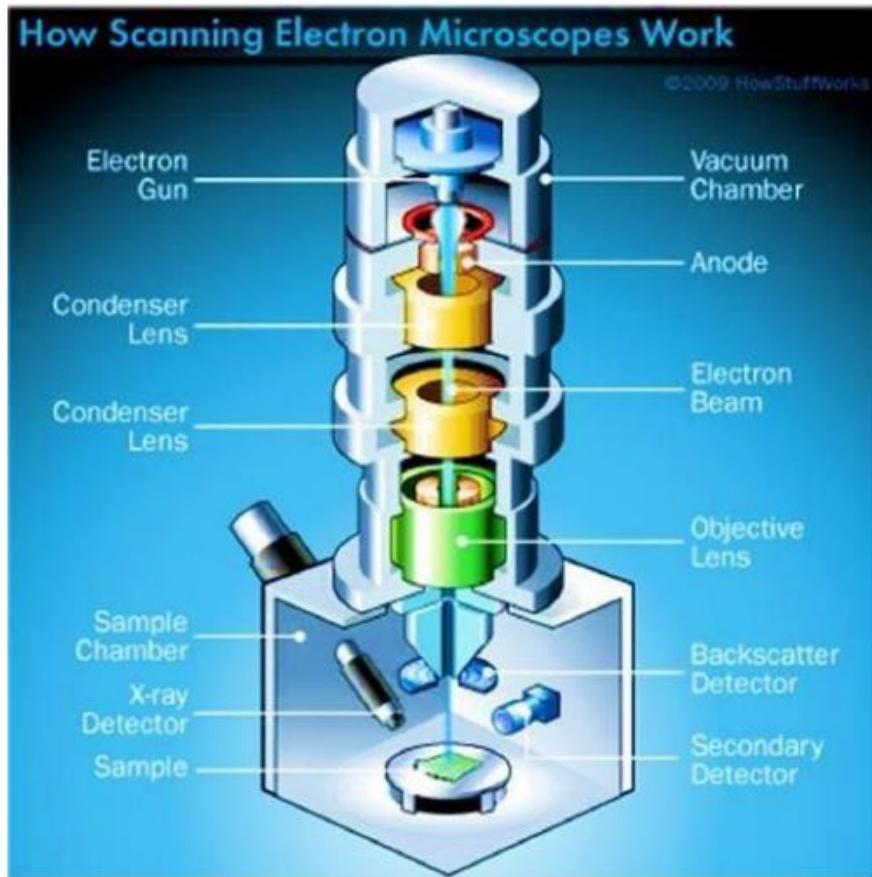


Figure 12: Illustrative diagram of SEM components

### 1.8.1.1 Working Principle

An electron gun generates high energy electrons, which are directed to fall on the sample surface. These electrons interact with that sample as shown in the figure, including:

- Auger electrons
- Backscattered electrons
- Diffracted backscattered electrons
- Secondary electrons
- X-rays etc

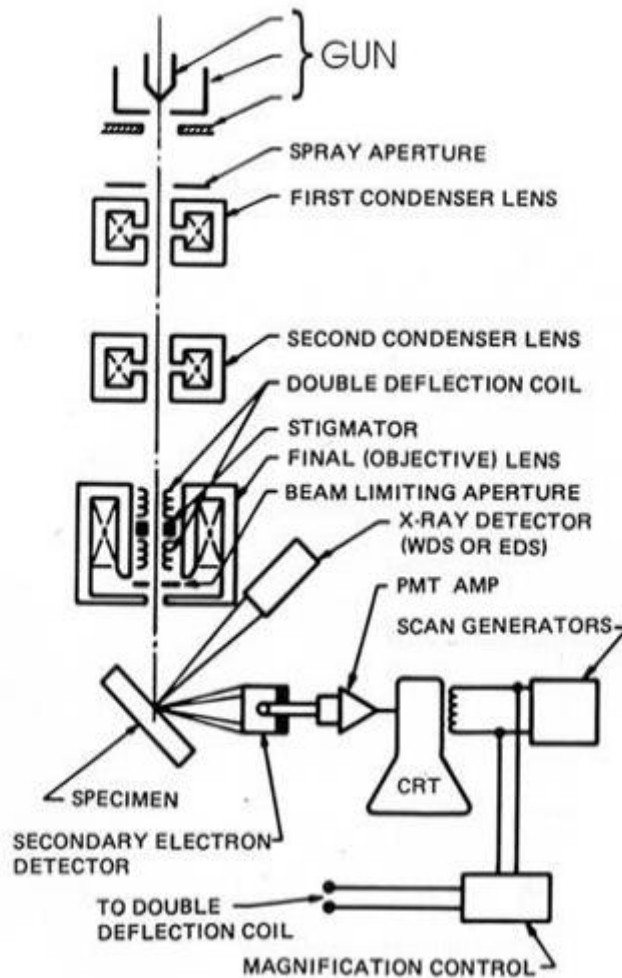


Figure 13: Working of Scanning Electron Microscope

The energy possessed by backscattered electrons lies closer to incident beam energy. The backscattered and secondary electrons are responsible for generation of SEM images. They cause differentiation between samples of different compositions in multiphase analysis. During de-excitation of these electrons, characteristic X-rays are produced.

### 1.8.2 X-Ray Diffraction (XRD)

X-ray diffraction technique, often referred to as crystallographic analysis, is used to analyze the crystalline nature of material. It possesses a key role in industrial as well as academic research. It is a non-destructive technique exhibiting information about several crystalline phases, quantitation as well as metrics of a unit cell. Several peaks appear in the resultant plot, due to constructive interferences of X-rays due to set of lattice planes at a specified angle. X-rays are capable to cover a range of 0.01nm to 10nm in an electromagnetic spectrum.

### 1.8.2.1 Working Principle

X-rays coming from heavy metal source are directed on to target crystals, resulting in the diffraction of rays. Electrons present at different points of atom in a unit cell cause the scattering of rays. Whenever there comes a regularity in a scattering center, resultantly wavelength of X-rays gets matched with the inter layer difference. Hence the rays after striking, reflect back through the planes. Interferences occur, that maybe constructive or destructive, that leads to different diffraction patterns [81].

Diffraction of X-rays through crystal layers are explained by Bragg's law by the following equation:

$$n\lambda = 2d_{hkl}\sin\theta_{hkl}$$

So just by knowing the wavelength of X-rays and their diffraction angle, we can calculate the spacing between lattice planes, unit cell metrics and miller indices by using above mentioned formula [82].

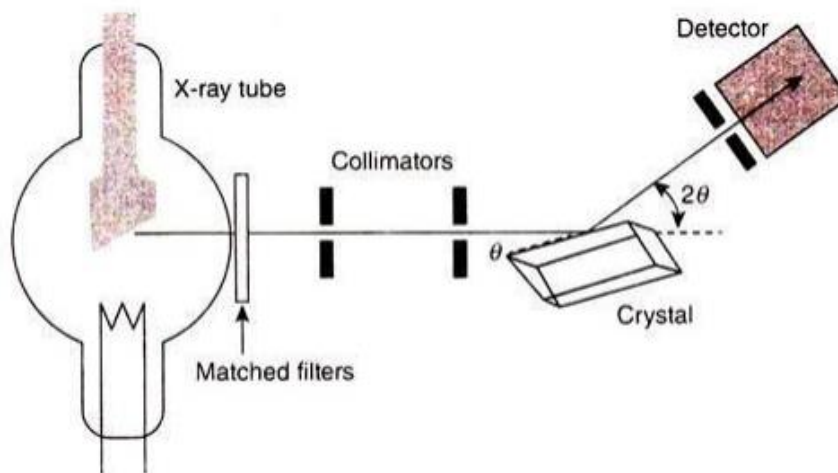


Figure 14: Illustrative diagram of operations of XRD

### 1.8.2.2 Instrumentation

The three major parts of XRD instrument, as presented in figure are as following:

- X-ray tube
- The sample stage
- Detector

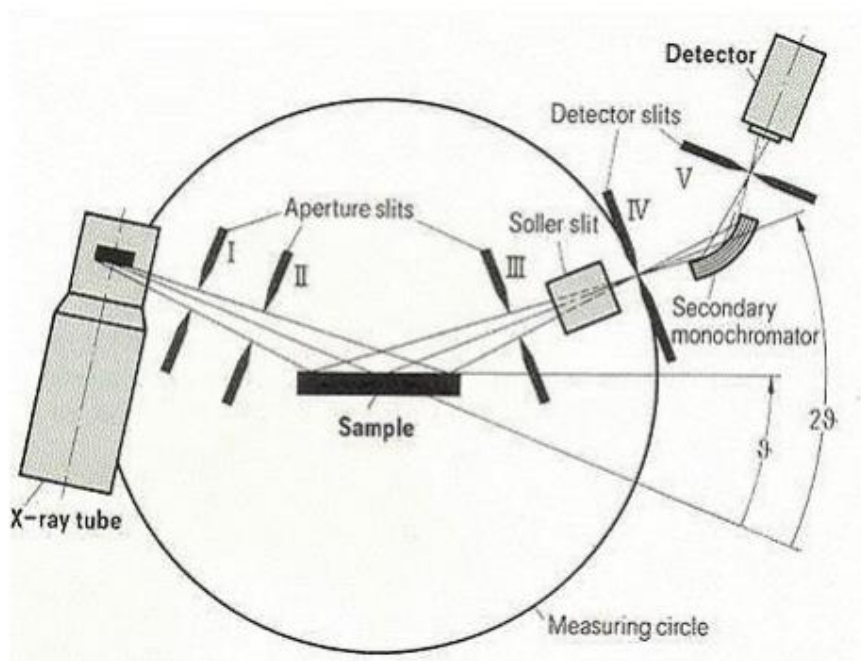


Figure 15: Instrumental diagram of X-ray Diffraction

### 1.8.3 BET- Surface Area Analysis

This analytical technique is based on BET theory, which was put forward by Stephen Brunauer, Paul Emmett and Edward Teller in 1938AD, hence named after them as Brunauer-Emmett-Teller (BET) theory that aims to estimate the surface area of a material by physical adsorption of gas molecules on its solid surface. Such an observation is often referred to as physi-sorption or physical adsorption. This theory was actually extension of Langmuir theory. Adsorption is defined as adhesion of atoms or molecules of a gas to a surface. It is a different phenomenon to that of absorption, in which a liquid permeates a solid or a liquid surface. Adsorption of a gas depends upon area of surface exposed to gas, pressure of gas, system temperature and the strength of interaction between solid surface and gas particles.



Figure 16: Micromeritics BET surface area analyzer

### 1.8.3.1 Working Principle

In surface area analysis by BET, usually nitrogen gas is used, because of its easier availability in highly pure state and it has a strong interaction with most of the solid surfaces. First of all the surface is cooled enough by using liquid nitrogen, to get detectable amount of adsorption. Then known amounts  $N_2$  gas are released stepwise into the sample cell. After when saturation pressure is attained, no more adsorption takes places, regardless of any further increase in pressure. Highly accurate and precise pressure measuring transducers monitor the changes in pressure, occurring due to adsorption or desorption process. When an adsorption layer is completely developed on the sample, it is then removed from nitrogen pressure and is heated so that nitrogen gas can get released from the surface of material and be quantified. Results are displayed in the form of a plot drawn between the amounts of gas adsorbed as a function of relative pressure. Resultant plots are also named as BET isotherms.

“Surface area of the sample is calculated by the following equation:

$$\frac{1}{X\left[\left(\frac{P_0}{P}\right) - 1\right]} = \frac{1}{XmC} + \frac{C - 1}{XmC} \left(\frac{P}{P_0}\right)$$

Where X is the mass of N<sub>2</sub> gas adsorbed at a relative pressure P/P<sub>0</sub>, X<sub>m</sub> is the volume of gas adsorbed at STP, and C is constant.

### 1.8.4 Cyclic Voltammetry

Cyclic voltammetry (CV) is an analytical technique, which is commonly used to study the processes taking place on an electrode surface [83]. This technique is used to study about factors affecting oxidation reduction reactions and their mechanisms. CV is usually performed for corrosion studies, sensing applications, redox reactions and environmental pollutants degradation studies.

#### 1.8.4.1 Working Principle

In CV analysis, the applied voltage is ramped linearly from already defined initial scan limit to final scan limit at a specified scan rate. When the final scan limit is attained, voltage is ramped in the opposite direction to the initial scan limit. Results obtained in the form of plot are called as voltammogram.

### 1.8.5 Impedance-Capacitance Analysis

It is an analytical tool used to analyze impedance capabilities and capacitance properties with respect to varying frequency range of zero hertz to several kilohertz. The electrical instrument used for its analysis is called as impedance analyzer. It is a type of electrical equipment which is used to measure complex electrical impedance as a function of test frequency. Impedance measured by this instrument is an important parameter used to characterize electronic components, electronic circuits, and the materials used to make components for electronics. This analyzer is also used to characterize materials exhibiting dielectric behavior such as food stuff, biological tissues or other geological stuff.

Impedance analyzers generally come in three distinct hardware implementations, and together these three implementations can probe from ultra-low frequency to ultra-high frequency and can measure impedances from μΩ to TΩ.



---

## Aims and Objectives

---

- To synthesize zeolite-based catalyst for electrochemical studies.
- To enhance its surface activity by doping with some other materials, to make it active for electrochemical responses.
- To study the chemistry of as-synthesized catalyst by employing various analytical characterization techniques.
- To analyze various electrochemical properties of this as-synthesized zeolite based catalytic material.

---

## Chapter 2 – Literature Review

---

This chapter aims at reviewing the available material, literature, methodology, techniques and apparatus involved in the splitting of water by zeolitic catalysts.

Zeolites are used for a number of applications like for removal of hardness of water, as catalysts for a large number of organic conversions, for petrochemical cracking, as a template for several other catalysts, electrochemical sensors and many more.

G. Hagen et. al. in 2006 presented their work by coating gold interdigital capacitor (IDC) electrodes with platinum doped Na-ZSM-5 zeolite thick sheets, they were able to produce highly sensitive and selective hydrocarbon gas sensors. The new exceptional sensor effect is due to a chromium (III) oxide layer between gold and zeolite. Diffusion of the chromium bonding agent through the gold electrode during annealing of the zeolite layer, followed by oxidation or deposition of additional  $\text{Cr}_2\text{O}_3$  layers on top of the electrodes using thin-film techniques, could generate such Au/ $\text{Cr}_2\text{O}_3$ /zeolite interfaces. High-frequency semicircles and low-frequency Warburg-like contributions make up impedance spectra. The hydrocarbon concentration in moist oxygen/nitrogen mixtures was shown to be extremely selectively dependent on the impedance at a fixed frequency in the low-frequency range. Cross-sensitivities to CO,  $\text{H}_2$ , NO, and  $\text{CO}_2$  gases were found to be very low or non-existent. Different substrate materials and  $\text{Cr}_2\text{O}_3$  layer thicknesses were examined. They presented a simple fundamental similar circuit concept [85].

K. Praveena et. al. in 2013 worked on the study of dielectric properties of dehydrated zeolites. They synthesized zeolite by microwave hydrothermal technology. And after sintering them to subjected temperatures, and characterizations, they were tested for DC current conductivity. It was found that DC conductivity was affected by the variation in annealing temperature. As zeolites contain several mobile cations, which are loosely bonded to nearby atoms, hence result in conductivity and other electrical properties [86].

In 2013 E. Parvez et al discussed the effect of rare earth metals on electrochemical properties of ferrites. It was found that by addition of a series of concentrations of  $\text{Gd}^{3+}$  ranging from 0.0 to 0.1 immensely effects the dielectric properties of ferrites. A prominent change in geometry appeared in ferrite structure, as trivalent Gd replaced Fe ions. along with change in structure,

dielectric properties were also affected. A decrease in tan loss at 1 GHz was observed in doped samples as compared to pure Co-ferrite sample. Magnetic properties also get affected by increasing amount of Gd [87].

M. Mahabole in 2014 studied the dielectric and ethanol sensing properties of ZSM-5 zeolite in nano sized state. These crystals were synthesized using microwave assisted hydrothermal technology without using organic template. Surface morphology was studied by using various analytical techniques like XRD, FTIR and TGA etc. sensitivity of ZSM-5 nano-particles towards ethanol was tested by a home made gas sensing unit. Ethanol injected on the thick film of ZSM-5 was sensed by plotting the resistance of film against temperature and voltage across the film was noted. Sensing capacity was estimated by comparison of resistance. Other electrochemical properties were also studied before and after injection of ethanol onto the film. It was found that conductivity of film was enhanced due to addition of ethanol into porous surface of zeolite. OH group of ethanol after entering into channel of ZSM-5, showed a greater activity due to high electron mobility resulting in higher electrical conductivity. Porous surface of zeolite is an important factor that decides that desorption taking place at nano scale can be sensed and porosity provides large surface to volume ratio for adsorption. Nano-ZSM-5 zeolite film gave response to 100 ppm ethanol within 150 seconds. The developed sensor was able to sense ethanol as minimum as 25 ppm [88].

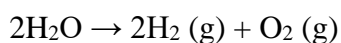
Xiumin Li et al in 2016 stated that hydrogen is an ideal replacement for the fossil fuels in future, because of its no emission of carbonaceous species during its use. Electrolysis of water is a dependable link of primary renewable energy and stable hydrogen energy. They reviewed popular electrocatalysts synthesized for both anodic oxygen evolution reaction (OER) and cathodic hydrogen evolution reaction (HER) and found that effective catalysts for HER include metal carbides, phosphides, chalcogenides and metal-free material, noble metals, non-noble metals and their composites, noble metal free alloys. On the other hand, for anodic OER reaction include Ni-based, Co-based materials and layered double hydroxides. Other than this, major challenges for the development of catalysts in future were discussed [89].

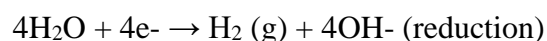
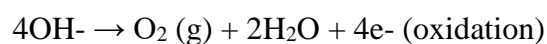
In 2016, A. M. Gashimov et. al. studied the dielectric parameters of composites based on electric discharge processed natural zeolites. They studied the influence of an electric discharge on the electrophysical parameters of composites based on discharge-processed natural zeolite and unprocessed polyethylene. Dielectric parameters of the material were reported and was found that electric charges change the electrophysical parameters of zeolites along with the

changes in its structure. Other than this, the electric discharge on zeolite makes it easier to trace the evolution of adsorption, being a natural adsorbent. As the processing time increases, the crystallinity of the samples increases, and new holes form, potentially improving the adsorbent's cleaning capacity. The electrical discharge alters the structure as well as the electrical properties of the natural adsorbent–polyethylene composite. It might be claimed that using an electrical discharge is the most cost-effective technique to improve the composite's adsorptive capacity [90].

S.F. Anis et al in 2018 mentioned that zeolites are often used as support for metals and metal oxides due to their high surface area and well-defined micro-porous structure. These are useful materials for redox reactions. They possess highly interconnected channel system having pore size of molecular dimensions along with having enough thermal stability. Main applications that zeolites find are as adsorbents, in separation and purification of gases molecular sieves in petroleum refining, catalytic cracking, and as ion exchangers for waste water purification on domestic and industrial scale. Apart from these, zeolites also find application in the field of energy production, such as hydrogen production through water splitting. Hydrogen is known to be fuel for the future, as it can be produced from an abundant source that is water and has more energy storage capacity as compared to oil. In this paper, two different loadings of WO<sub>3</sub> were studied, 3% and 5% by wt. with respect to overall catalyst. These loadings brought changes in electrochemical activity of catalyst. The over potential and Tafel slopes were decreased with 3% loaded zeolite, however on increasing the load upto 5%, a decrease in performance was observed, primarily due to low surface area, and greater effect of WO<sub>3</sub> on HER, rather than synergic effect of zeolite-WO<sub>3</sub>. It was concluded from this study that due to a small metal oxide addition, nano-zeolite started showing superior performance, which is attributed to its size and resultantly easy escape of hydrogen bubbles from catalyst [91].

In a paper by Jadranka et al explained about water splitting in the presence of nickel doped zeolite catalysts in an alkaline medium. Reportedly this process is not thermodynamically feasible because of high amount of energy required to split water molecules. Large over potential is required by oxygen evolution reaction (OER) at anode and hydrogen evolution reaction (HER) at cathode to proceed at a reasonable rate. Therefore, highly active electrocatalysts are required for these two reactions, possessing large active surface area, high selectivity and electrochemical stability, corrosion resistant and of low cost.





They investigated the electrochemical activities of zeolite-based nickel derivatives wise NiA and NiX, as electrochemical catalysts, and found that NiA has higher electrochemical activity for both HER and OER. Both catalysts were found enough stable when tested through chronography. The HER is controlled by the adsorption of the Hads intermediate in the case of NiA, while the total resistance associated to the HER is lower for NiA than for NiX, according to the impedance data. In the case of the OER, on the other hand, the charge transfer controls the impedance response [92].

Juan Wang et al in 2019 studied the effects of amorphization of crystalline catalysts on electrochemical water splitting. Amorphization means to remove regular repetition in the structure of a material. They synthesized nano rods of ruthenium-tellurium. They observed that theoretical calculations identify the local distortion-strain effect in amorphous RuTe<sub>2</sub> system hence abnormally sensitizing the Te-p $\pi$  coupling capability and enhances the electron transfer of Ru-sites, in which the excellent inter-orbital p-d transfers determine strong electronic activities for boosting OER performance. Thus, a robust electrocatalyst based on amorphous RuTe<sub>2</sub> porous nanorods (PNRs) was successfully fabricated. In the acidic water splitting, a-RuTe<sub>2</sub> PNRs exhibit a superior performance, which only required a cell voltage of 1.52 V to reach a current density of 10 mA cm<sup>-2</sup>. Detailed investigations showed that the high density of defects combine with oxygen atoms to form RuO<sub>x</sub>H<sub>y</sub> species, which are conducive to the OER. Hence resulting in a new head start in the domain of catalyst synthesis for energy production [93].

M. Lakhane et al in 2019 explored the dielectric properties of zeolites and their composites. They synthesized composites of various metal oxides nanoparticles. Concentrations of nanoparticles were varied wise 25%, 50%, 75% by weight, and added to the parent material. It was found that dielectric properties depend upon the type and concentration of nanoparticles of metal oxides. All composites were found having higher dielectric permittivities as compared to ZSM-5 zeolite. Composites showed a gradual decrease in dielectric constant values with increase in metal oxides nanoparticles concentration. Highest dielectric constant was found in composite having 25% concentrations of ZnO, TiO<sub>2</sub> and CuO metal oxide content. Along with this, dissipation factors were also found to be lowered. The AC conductivity remained constant

in low frequency region and increased linearly at higher frequencies. Composites blended with CuO nanoparticles were found to be showing extremely high dielectric values [94].

S.A. Pullano et. al. in 2020 worked on the synthesis of affordable zeolite based capacitor for gas sensing properties. Due to its intriguing adsorption/desorption characteristics, zeolite is a kind of material that has gotten a lot of attention in a variety of applications. The behaviour of a zeolite-based capacitive sensor for the adsorption of dry air, N<sub>2</sub>, NO, and C<sub>2</sub>H<sub>4</sub>F<sub>2</sub> was examined in this study. The pore width and structure dimension of the zeolite are important factors in optimizing adsorption capabilities, which results in different variations in permittivity. The dielectric characterization of samples manufactured with zeolite 4A and soybean oil combination demonstrated that inexpensive gas sensors may be made using a simple fabrication approach that does not require the use of specific chemicals or reagents. The gas species affects the sensor differently depending on the gas molecule, as demonstrated by the electric characterization. The sensitivity was -1.3 pF/bar (N<sub>2</sub>), -1.3 pF/bar (NO), to 10.9 pF/bar (dry air) and 18.6 pF/bar (C<sub>2</sub>F<sub>4</sub>H<sub>2</sub>). Higher changes in capacitance were shown when the negatively charged tetrahedra of the zeolite crystal framework were exposed to dry air (C/C<sub>0</sub> = +4.2%) and 1,1-difluoroethane (C/C<sub>0</sub> = +7.3%), while lower dielectric variations were found upon exposure to nitrogen (C/C<sub>0</sub> = -0.4%) and nitric oxide (C/C<sub>0</sub> = -0.5%). The behaviour of capacitance versus pressure was discovered to be similar to that of a low-pressure adsorption isotherm with a low Langmuir constant. In fact, data fitting revealed linearity of >0.99. A simple fabrication technique, according to the proposed technique, could allow a convenient and economical realisation of reusable capacitive gas sensors [95].

V. Abdelsayed et. al. in 2020 studied the interaction of microwaves with the zeolites during non-oxidative coupling of methane. For non-oxidative methane conversion processes, the interaction between microwave energy (2.45 GHz) and ZSM-5 zeolites of varied surface acidity was investigated. The reactions were carried out at 700 degrees Celsius, 1200 scc/g/h, and atmospheric pressure. Bronsted acid sites are critical in microwave catalyst design employing zeolite-based catalysts, according to the findings. The zeolite with the lowest acid site concentration (H280) did not interact with microwave energy at all, resulting in no methane conversion. Increased acid sites on the surface via dipole polarization from -Al(OH)- Bronsted acid groups, followed by a contribution from conduction polarization losses due to poly-aromatic coke deposits on the surfaces, increased the extent of microwave coupling with a zeolite catalyst. Surface acidity boosted methane conversion to hydrogen, C<sub>2</sub>, and benzene. Under the same temperature, surface acidity, and reaction conditions, the conventional thermal

approach converted more methane into carbon and coke than the microwave approach. When compared to traditional thermal samples, the microwave MW-H23 sample demonstrated increased production rates for hydrocarbons and aromatic compounds. Only a highly acidic zeolite catalyst produced acetylene under microwave and ordinary heating [96].

Haojie Zhang et al in 2020 reported that cost of reducing greener hydrogen production is necessary for the development of a hydrogen fuel-based economy. Thus, development of cost effective electrocatalysts for electrolysis of water is of a great research interest. Among candidates of various materials, transition metal phosphides (TMP) have proved to be robust bifunctional electrocatalysts for both oxygen evolution reaction (OER) and hydrogen evolution reaction (HER) due to their various phases and variable electronic structure [97].

According to the heterostructure idea, combining two active catalysts can considerably increase their catalytic activity due to the synergistic effect of the interface between the two components. Multiple contributing aspects, such as bubble formation and release, wettability, the number of active sites, and the electrical structure of the heterointerface, complicate the synergistic effects that occur on the heterointerface [98, 99].

---

# Chapter 3 - Materials and Methods

---

## 3.1 Instruments

Hot plates, heating oven, chamber furnace, micropipette, sonicator and some other instruments were used during synthesis and electrodes preparation procedure.

## 3.2 Chemicals

All the chemicals used in this catalyst synthesis were of analytical grade. Because the concept behind the synthesis was to make it greener, so not a single solvent was used in the whole synthesis, except water which was used just for washing purposes.

Table 2: List of chemicals

Chemical name	Chemical formula	Supplying company	%age purity
Ammonium chloride	NH <sub>4</sub> Cl	Sigma Aldrich	98%
Sodium silicate	Na <sub>2</sub> SiO <sub>3</sub> .9H <sub>2</sub> O	Sigma Aldrich	98%
Silica gel	SiO <sub>2</sub>	Sigma Aldrich	99%
TPABr	C <sub>12</sub> H <sub>28</sub> NBr	Sigma Aldrich	98%
Aluminum hydroxide	Al(OH) <sub>3</sub> .xH <sub>2</sub> O	Sigma Aldrich	57%
Deionized water	H <sub>2</sub> O	Merk	100%
Cerium(III) nitrate	Ce(NO <sub>3</sub> ) <sub>3</sub> .6H <sub>2</sub> O	Daejung	100%
Zirconium(IV) nitrate	Zr(NO <sub>3</sub> ) <sub>4</sub> .4H <sub>2</sub> O	Daejung	100%

---



### 3.3 Experimental Work

Synthesis of ZSM-5, its composites with Cerium and Zirconium salts was carried out in lab and characterized by various analytical instruments. Complete procedures of their synthesis and electrode formation for water splitting is explained in this section.

This method of catalysts synthesis can also be named as solvent free synthesis of ZSM-5 catalyst. As during this whole procedure, not a single solvent is used, except water. Which is also used in a very small amount for just washing purposes.

#### 3.3.1 ZSM-5 Synthesis

Synthesis of Zeolite Socony Mobil (ZSM-5) was started by mixing solid  $\text{SiO}_2$  (0.60 g, 10.0 mmol),  $\text{Na}_2\text{SiO}_3 \cdot 9\text{H}_2\text{O}$  (2.64 g, 9.3 mmol), TPABr (0.48 g, 1.8 mmol),  $\text{Al}(\text{OH})_3 \cdot x\text{H}_2\text{O}$  (0.05 g, 0.64 mmol) and  $\text{NH}_4\text{Cl}$  (0.82 g, 15.3 mmol) in a mortar. The whole mixture was grinded with a mortar, for about 20 minutes, until a solid paste is formed. This whole mixture was transferred to a Teflon lined autoclave for thermal treatment at  $180\text{ }^\circ\text{C}$ , in a heating oven. After 48 hours of thermal treatment, the product was taken out and washed once with deionized water. After washing, it was dried at  $80\text{ }^\circ\text{C}$  for an hour, in an oven. Then this dried powder was transferred to a ceramic crucible and placed in a chamber furnace. The product was calcined at  $550\text{ }^\circ\text{C}$  for 6 hours under air flow. After calcination, final product was obtained as calcined ZSM-5 zeolite.



Figure 17: Paste like appearance of materials after grinding

### 3.3.2 Doping

For synthesis of doped ZSM-5, the sorption method was used. Zirconium and Cerium salts were added during the initial mixing to form Zr-ZSM-5 and Ce-ZSM-5 respectively. 1 gram of each salt was added, and the whole mixture was ground thoroughly to form a homogenous paste. The composite ratio was 1:4 by mass. Then the rest procedure same as that of ZSM-5 synthesis was repeated. After hydrothermal treatment, washing and calcination, Zr-ZSM-5 and Ce-ZSM-5 powders were obtained.

### 3.3.3 Conditions for Characterizations

X-ray diffraction analysis of powder of ZSM-5 and its composites was done in 2 theta ranging from 5 to 80 degrees.

Scanning electron microscopic analysis was performed at several resolutions, using 10 keV electron gun source, revealing the microstructure of ZSM-5 and its doped materials.

Surface area analysis was done by Micromeritics Gemini VII 2390 V1.03. Conditions for samples analysis are mentioned in the table:

Table 3: Conditions for BET analysis

Analysis Adsorptive	N2
Equilibration Time	5s
Sat. Pressure	760.00 mmHg
Sample Mass	0.150 g
Sample Density	1.000 g/cm <sup>3</sup>
Evacuation Rate	1000.0 mmHg/min

### 3.4 Pellets preparation for impedance capacitance analysis

All the three samples were ground to finely powdered form. Grinding was done by pestle and mortar for an hour. After grinding, these samples were dried in vacuum oven at 80°C for about an hour. After drying these samples were transferred to dyes individually for pellet making. Pellets were made by hydraulic pellet maker by using 5 tons per 13mm pressure. After

preparation, these pellets were sintered at 400°C for about 4 hours. Then these sintered pellets were further proceeded with impedance and capacitance analysis. Pictures of pellets of all the three samples are shown in figures below.



Figure 18: Pellet of pure ZSM-5



Figure 19: Pellet of Zr-ZSM-5 composite



Figure 20: Pellet of Ce-ZSM-5 composite

### 3.5 Impedance Capacitance Analysis

Pellets as prepared by above mentioned method were subjected to Wayne Kerr 6500B, precision impedance analyzer. Frequency range in which the dielectric properties were tested was from 100 Hz to 400 Hz. After obtaining results of impedance and capacitance variables, with respect to frequency range, further calculations were done, and plots were drawn.

### 3.6 Electrode Preparation for CV

Three electrodes unit was used for electrode and electrolytic studies.

**Reference Electrode:** Ag/AgCl electrode was used as a reference electrode.

**Counter Electrode,** which was composed of a platinum wire measuring surface area of approximately  $1\text{cm}^2$ .

**Working Electrode:** And the third one was working electrode which was prepared in lab. It was prepared on fluorinated titanium oxide (FTO) glass slides. Rectangular slides of  $2\text{cm}^2$  area were obtained. Slides were first washed and sonicated in deionized water, analytical grade ethanol and acetone respectively for 15 minutes in a sonicator. After those slides were allowed to dry in oven at  $80\text{ }^\circ\text{C}$ . After that, a slurry solution of all the materials to be deposited on the slides were prepared. 0.010 g of each sample powder was mixed in 1 ml of ethanol in a sampling vial. These mixtures were placed in sonicator for about 15 minutes, so that a uniform slurry mixture could be obtained. After that, dried FTOs were placed on a hot plate by setting its temperature to  $80\text{ }^\circ\text{C}$ . By using micropipette, those slurry mixtures were transferred to FTOs,

by using separate pipette needle for every mixture. Then those FTOs were allowed to dry for about 10-15 minutes, and then were proceeded with further electrochemical studies.

### **3.7 Electrolyte Preparation**

1M KOH solution was used as electrolyte for running basic operations of electrochemistry. Solution was prepared by dissolving 56.10 grams of KOH in deionized water to prepare 1L solution. Then this solution was used as stock of electrolyte for studies.

### **3.8 Electrochemical Operations**

In cyclic voltammetry operations. Potential ranging from 1 to -1 was applied at the scan rate of 50mV/s. The graph of potential versus current obtained was drawn and peak current calculations were done.

In impedance and capacitance operations, AC current was passed through sample at various frequency ranges. Results were obtained and various calculations were done to plot in the graphical form. Impedance capacitance analysis were done by Wayne Kerr 6500B Precision Impedance analyzer. All the three samples were firstly dried in a vacuum oven and then ground very finely by pestle and mortar for about an hour. Then samples were converted into pallet shapes by using manual punch dying molds and pill making punch machine. Then these pallets were calcined at 400°C for 4 hours. These calcined pallets were tested for impedance and capacitance by above mentioned instrument.

---

---

## Chapter 4 - Results and Discussion

---

---

ZSM-5 and its two composites were characterized by various techniques including XRD, SEM, FTIR and BET to evaluate the morphology and confirm the synthesis of desired samples. Electrochemical techniques including LSV and impedance and capacitance analysis were used for the study of dielectric and other electrochemical properties. Results of these analytical techniques are discussed in this chapter.

### 4.1 XRD Analysis

X-ray diffraction analysis was performed at SNS-NUST Islamabad, and results are shown in figures 21 and 22.

XRD data obtained from analysis of pure ZSM-5 powder, presented typical peaks of zeolite-based material. The most prominent peaks appeared at 7.8, 8.4, 23.0, 23.8- and 24.4-degrees values of  $2\theta$  confirming the typical structure of ZSM-5 as reported in the literature.

While the XRD plots of composites showed some other peaks of parent materials as well. Three additional prominent peaks appeared at 29.89, 50.39 and 60.2 degrees of  $2\theta$  values on the plot obtained from XRD data of Zr-ZSM-5 composite. While on the plot of Ce composite with that of ZSM-5, peaks appeared at several other positions. Those were at 28.2, 47.68 and 56.67. Independent peaks of doping materials showed that ZSM-5 being enough stable material does allow the change in chemistry of material. Rather Ce and Zr material molecules got adjusted in the pores of ZSM-5 and on the surface, as peaks of ZSM-5 are clearly visible in the X-ray diffraction plots of composite materials. A nominal difference has been observed in the intensity of crystallographic peaks, showing a notable decrease in crystallinity of composite materials, as compared to pure ZSM-5.

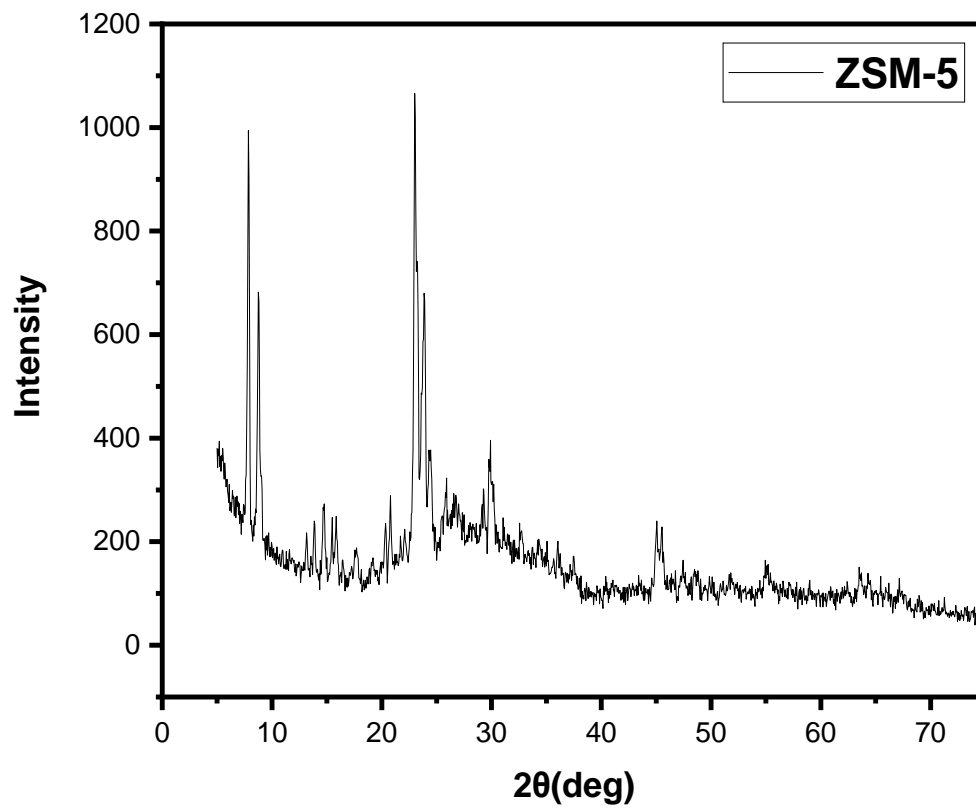


Figure 21: XRD results of ZSM-5

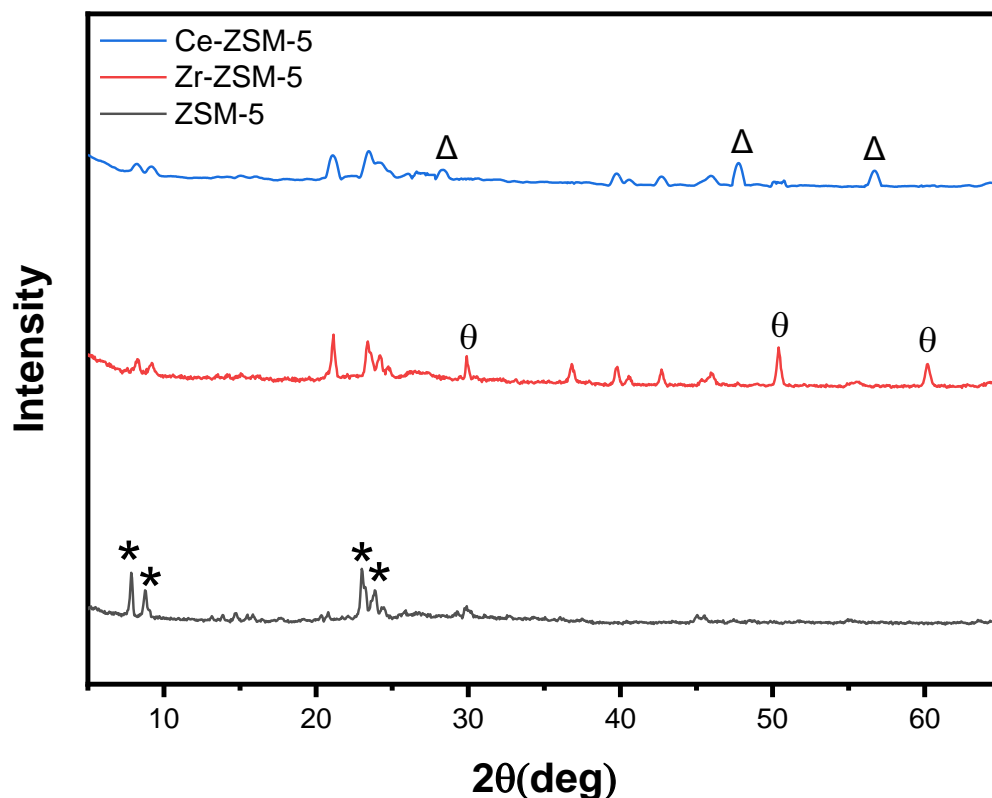


Figure 22: XRD comparative analysis of three samples

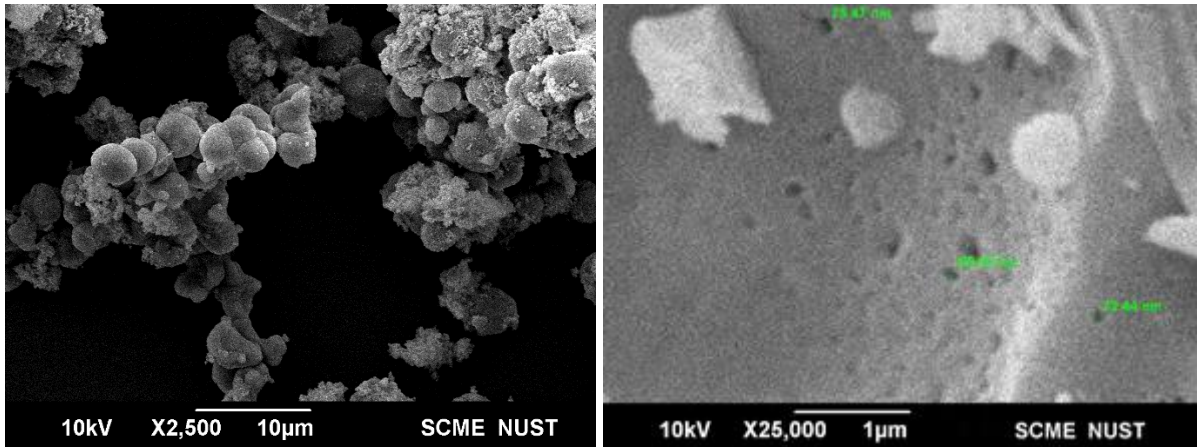
#### 4.2 SEM analysis

Scanning electron microscopic analysis was performed at several resolutions, revealing the microstructure of ZSM-5 and its doped materials.

SEM analysis revealed that ZSM-5 possesses a very highly porous structure. Pore size ranges from several nanometers to micrometers. When seen at lower resolution, it is found possessing regular uniform structure.

After addition of salts of cerium and zirconium it can be seen from the images that porosity level has decreased in both samples. Which shows that salts have adjusted into the pores of ZSM-5 zeolite.





(a)

(b)

Figure 23: Photograph of synthesized ZSM-5(a. Particles view b. Pores view)

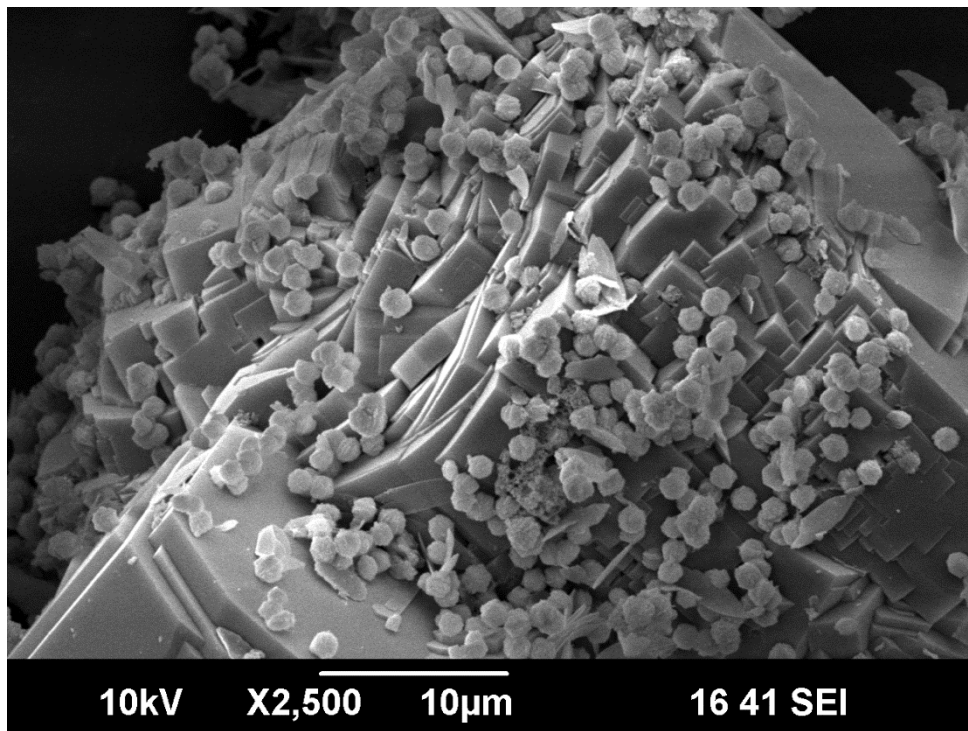


Figure 24: Photograph of synthesized Zr-ZSM-5

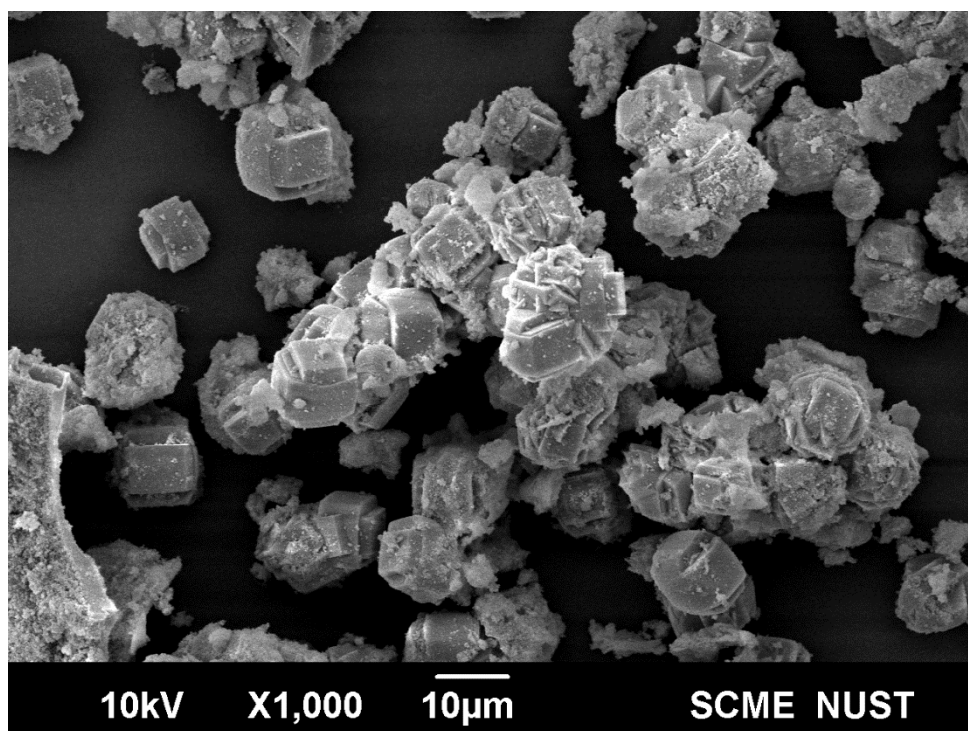


Figure 25: Photograph of synthesized Ce-ZSM-5

### 4.3 BET analysis

BET analysis results of ZSM-5 and its composites as produced by instrument, are presented in table below:

Table 4: Surface area analysis results

	ZSM-5	Zr-ZSM-5	Ce-ZSM-5
Single point surface area ( $p/p^0$ ) ( $m^2/g$ )	299.46	215.4356	195.9218
BET surface area ( $m^2/g$ )	268.95	177.5452	146.7996
Langmuir surface area ( $m^2/g$ )	423.58	343.0114	296.0797
t-Plot micropore area ( $m^2/g$ )	213.13	33.0326	--
t-Plot external surface area ( $m^2/g$ )	55.82	144.5125	--
BJH adsorption SA of 17-3000 Å wide pores ( $m^2/g$ )	37.958	116.621	132.432

Table 5: Pore volume analysis results

	ZSM-5	Zr-ZSM-5	Ce-ZSM-5
Total volume of pores less than 30.007 Å (m <sup>2</sup> /g)	0.147903	0.120246	0.103189
t-Plot micropore volume (m <sup>2</sup> /g)	0.119730	0.034461	--
BJH adsorption total vol. of pores 17-3000 Å wide (m <sup>2</sup> /g)	0.020902	0.074141	0.072708

Table 6: Pore size analysis results

	ZSM-5	Zr-ZSM-5	Ce-ZSM-5
Adsorption average pore width (4V/A by BET) (Å)	21.9967	27.0908	28.1169
BJH Adsorption average pore width (4V/A) (Å)	22.026 Å	25.430	21.961

Maximum surface area was found in ZSM-5, due to its hugely porous structure. Nanosized pores were observed on its surface. Surface area of catalyst was decreased, as an external transition metal salt was introduced in it. Decrease in total surface area indicates that, doped species have been adjusted inside the pores.

#### 4.4 FTIR analysis

Figure shows the FTIR analysis results of ZSM-5 synthesized by hydrothermal treatment of aluminosilicates mixture. Spectrum showing a very intensive absorbance band at 1100 cm<sup>-1</sup> represents insensitive and internal tetrahedron asymmetric stretching vibrations. Another band at 1400 cm<sup>-1</sup> represents silanol group in the structure. Meanwhile a characteristic band of double five ringed structure of MFI-type zeolites can be observed at 620 cm<sup>-1</sup>. Although the band at sub-nanocrystals at 620 cm<sup>-1</sup> is weak but may be a proof for the presence of primary structure of MFI type zeolite structure.

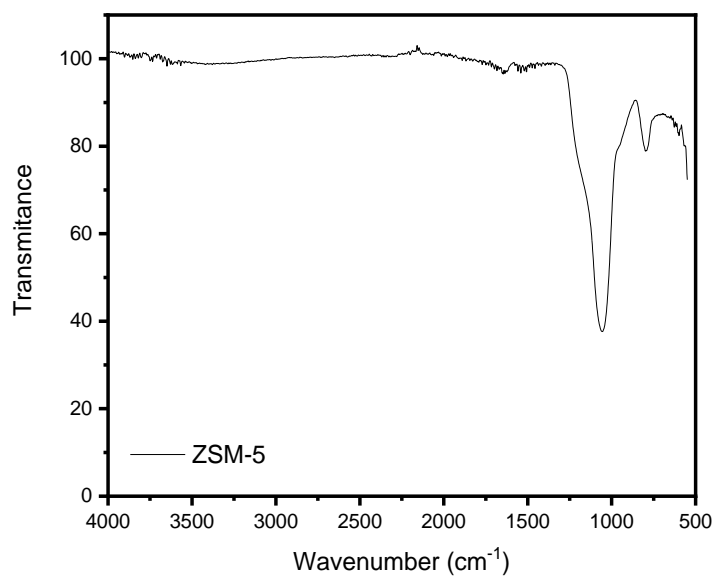


Figure 26: FTIR analysis of ZSM-5

Figure shows the FTIR analysis of Zr-ZSM-5. Spectrum shows all the constitutional bands of ZSM-5, proving that due to addition to Zr salt, no change in the structure of zeolite has taken place. But the decrease in intensity of bands presents the idea that crystallinity of sample has decreased, as justified by the surface area analysis as well. It assures the concept that the molecules of added salt have adjusted themselves in the pores of zeolite and have not disturbed the entire structure of zeolite.

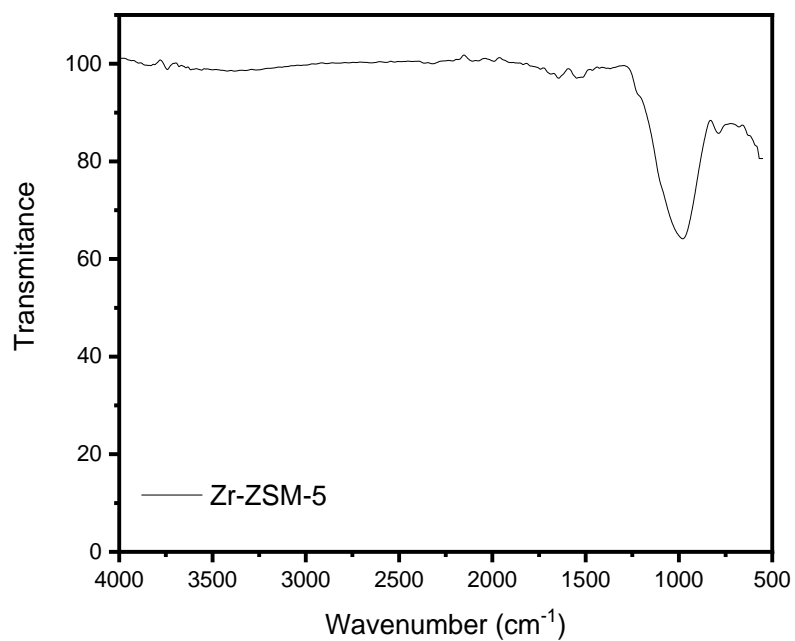


Figure 27: FTIR analysis of Zr-ZSM-5 composite

Figure represents the FTIR spectrum of Ce-ZSM-5. It is clear from the spectrum that all the absorptive bands represent the structure of zeolite. No appearance of no extra band shows that no bonding has been developed in between zeolite powder and Cerium salt. It has just adjusted into the pores of ZSM-5.

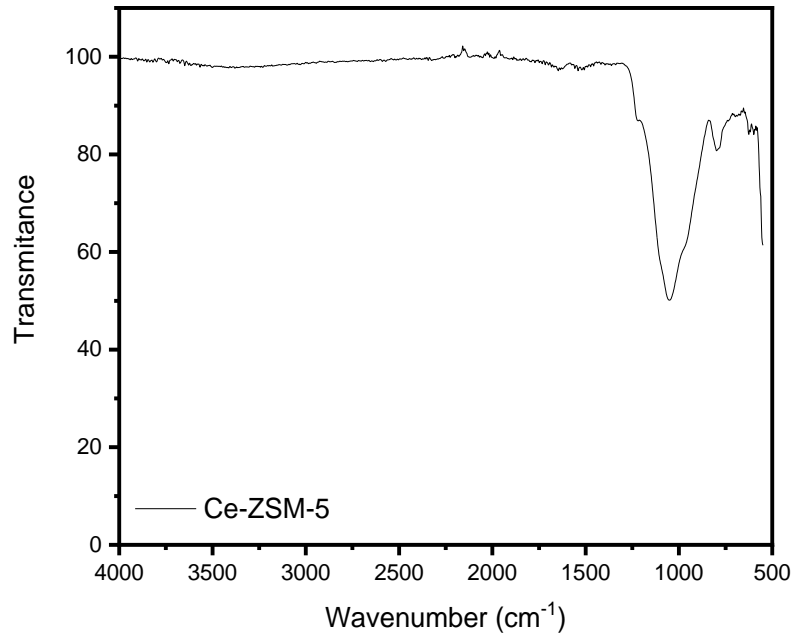


Figure 28: FTIR analysis of Ce-ZSM-5

## 4.5 Impedance Capacitance analysis

Several calculations were done with the data obtained from the instrument. And were plotted against natural logarithm of frequency.

### 4.5.1 Dielectric Constant study

Dielectric constant calculation was done by using equation:

$$\epsilon' = \frac{C \times d}{A \times \epsilon_0}$$

Where C is the capacitance of sample calculated by Precision impedance analyzer, d is the thickness of pallet, measured by vernier calipers, A is the area of cross section of the pallet and  $\epsilon_0$  is the permittivity of vacuum that is  $8.85 \times 10^{-12}$ . Plot was drawn between  $\ln f$  and  $\epsilon'$ .

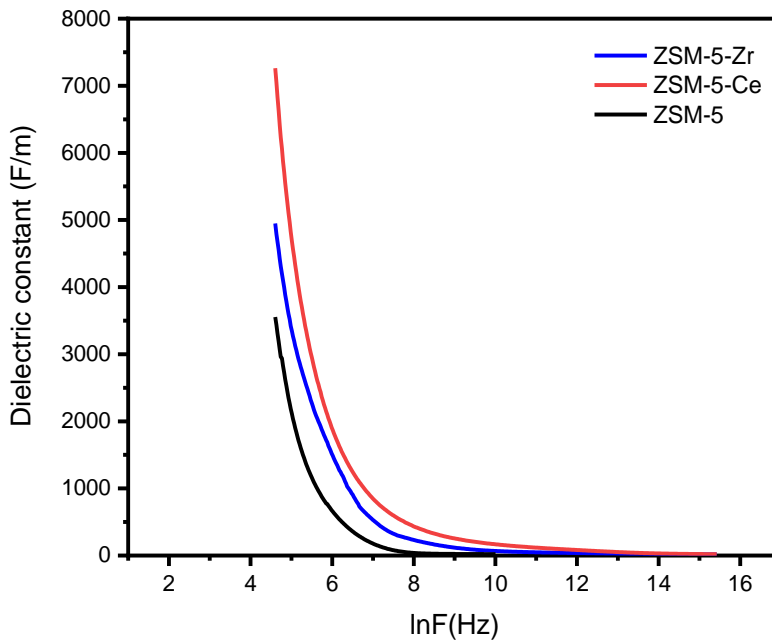


Figure 29: Plot of  $\epsilon'$  vs  $\ln F$

Figure 29 shows that maximum dielectric constant is shown at lower frequencies starting from approximately 4 to 7 Hz of  $\ln F$ . Highest constant value appears to be of Cerium salt doped ZSM-5 i.e. about 7500F/m, and least value is shown by pure ZSM-5. Which shows that doping has enhanced the dielectric property of zeolite powder. ZSM-5 itself possesses mobile ions in its porous, channels having structure. These ions are the reason for electrical conductivity and other dielectric properties.

When another ion is added to zeolite structure, it causes an increase in the electrical energy conducting ions. Cerium shows the better results because of having free electrons in their outermost shell, because its outermost three electrons are easily available for dielectric properties. Zeolite on the other hand shows minimum dielectric constant value, because of having its structural ions only.

#### 4.5.2 Dielectric loss

Dielectric loss determines the measure of energy dissipation during charging and discharging due to the movement of charges.

It is calculated as:

$$\epsilon'' = D \text{ factor} \times \epsilon'$$

Where D factor is calculated by precision impedance analyzer.

Figure shows that zeolite powders show maximum losses at low frequencies which go on decreasing and ultimately become constantly equal to zero. Highest energy dissipation appears to be occurring in ZSM-5 and lowest in cerium doped zeolite powder.

As zeolite powder only has structural free and mobile ions, along with these it possesses channels and pores in its structure. These channels offer hurdles on the pathway of electrons, causing enough number of losses in energy. When this structure is doped with Zr and Ce ions, they take place of these pores, hence resulting in prominent decrease in dielectric losses. Cerium doped ZSM-5 shows minimum losses of the three samples.

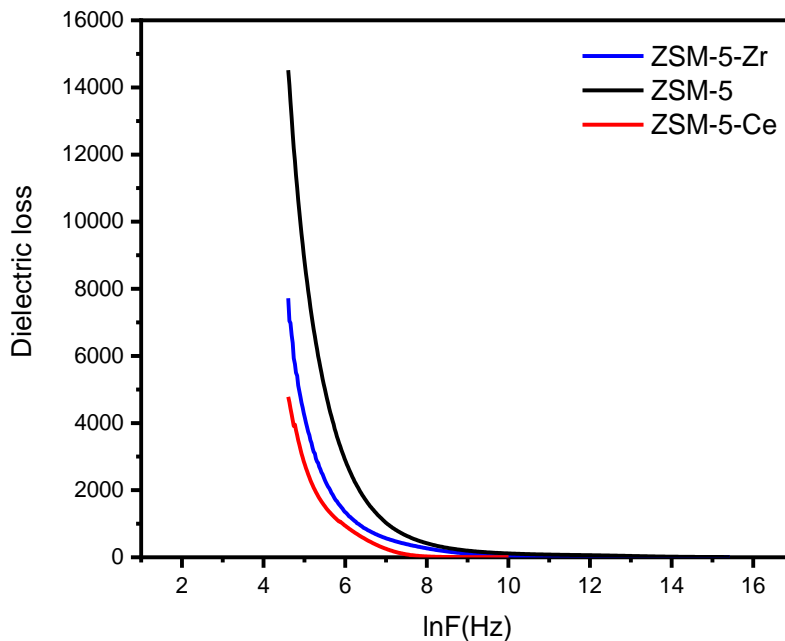


Figure 30: Plot showing relationship b/w Dielectric loss and lnF

#### 4.5.4 Sigma AC

Sigma AC refers to the frequency dependent alternating current conductivity. DC current is frequency independent but AC conductivity depends upon frequency of current. It refers to the movements of hopping electrons of materials.

It is calculated as:



$$\sigma_{AC} = 2\pi f \epsilon_0 \epsilon''$$

Where  $\sigma$  is the conductivity of alternating current and  $f$  is the frequency of current.

Conductivity of alternating current is plotted against  $\ln F$  and the results are shown in the figure below. All the samples show lower conductivity at lower frequency range, which goes on increasing by the increase in frequency of current. Highest conductivity is shown by Ce doped ZSM-5 powder and the rest two samples show nearly equal conductivities but at variable range of frequency. Because cerium has three valence shell electrons, which can be easily removed to become  $Ce^{3+}$  ion, resulting in the huge enhancement of conductivity. On the other hand, ZSM-5 shows least conductivity due to least number of ions present in their structure. ZSM-5 shows conductivity because of  $Al^{+3}$  ions present in its structure. Zr as compared to Ce has less number of free electrons in its structure, that's why showing less conductivity for AC.

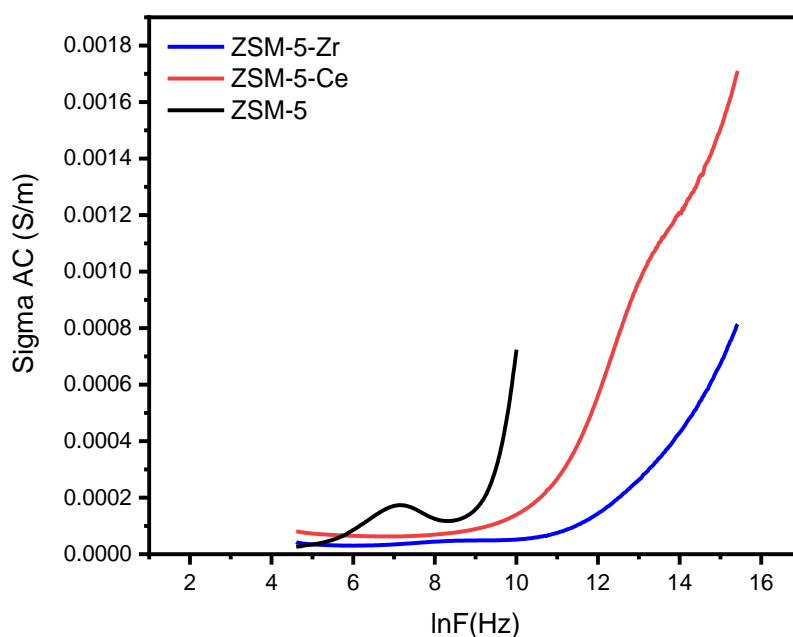


Figure 32: Plot of relationship b/w sigma AC and lnF

#### 4.5.6 Complex electric modulus

This portion refers to complex dielectric properties and their dependence on frequency. Figure 33(a) refers to relationship of real part with frequency variation and figure 33(b) refers to the comparison of imaginary part with the various frequency ranges.

A comparison of real part versus imaginary part of all the three samples. It represents the role of electron hopping in grain boundary and the grains itself. The two curves appearing in the results represent the two parts separately. The first semi circular curve represents the grain boundary affect and the second curve represents the grains effect.

As shown by the results in figure 34, the pure ZSM-5 sample shows maximum grains boundary effect which shows the reason of maximum losses in this sample. Grains effect of this sample is least of the three samples. As long as zeolite material is doped with the transition metal salts, there comes a prominent difference in activities.

In Zr doped material, there appears a small grain boundary curve and a dominant grains curve showing effective role of doping in energy storage process. In Ce doped ZSM-5 sample, there is a small grain boundary effect curve and a large grains effect curve. It actually shows the increase in number of conducting particles inside the zeolite matrix. Due to doping Ce and Zr ions are added into the matrix, so when a potential is applied, they conduct more as compared to the ions of zeolite. It is obvious that due to doping, dielectric properties have been enhanced enormously.

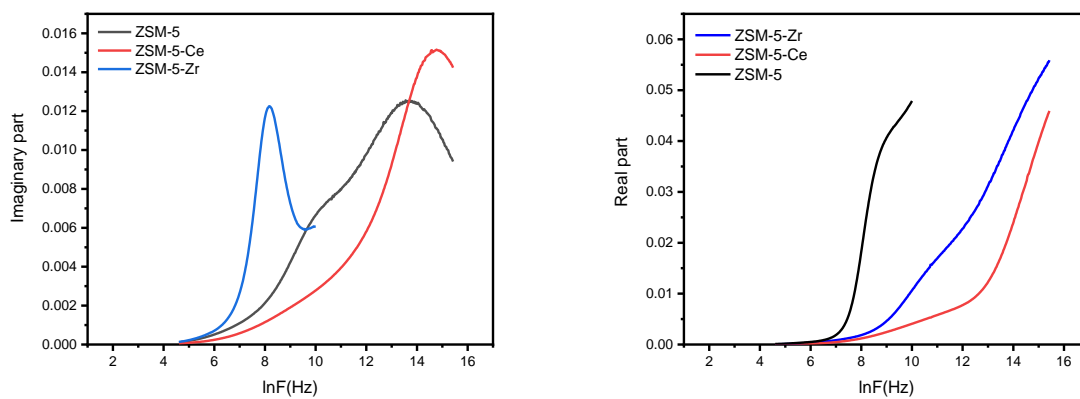


Figure 33: Complex dielectrics (a) Imaginary part (b) Real part

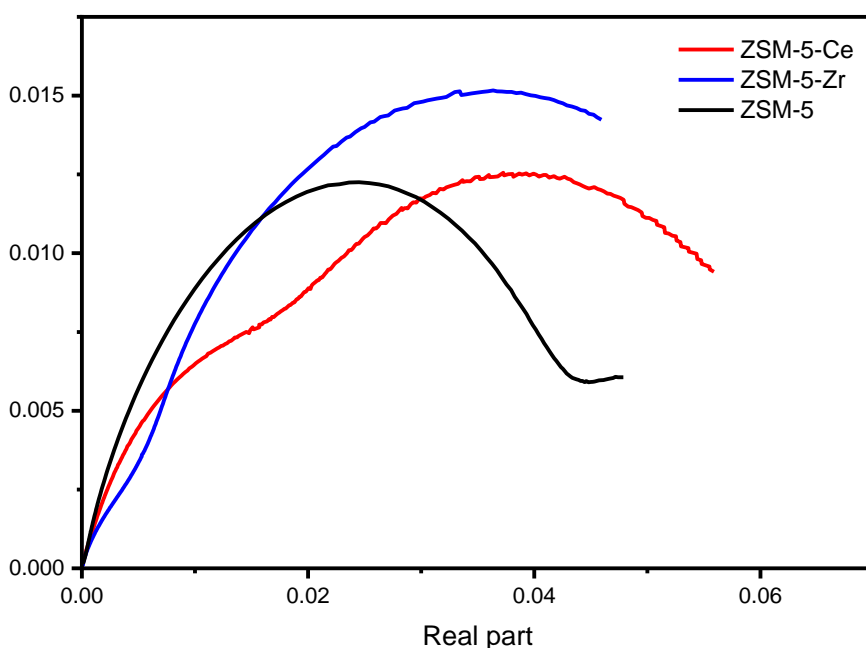


Figure 34: Cole-cole plots of samples.

#### 4.5.7 Quality factor

It refers to the ratio of energy stored by the capacitor to the energy dissipated during charging and discharging process by an alternating current based system. As it is the ratio of two energies, so there is no unit of Q-factor. All the three samples show least efficiency at lower frequency ranges. ZSM-5 shows better efficiency on lower frequency, but on a very short range of frequency i.e. from 8-9 of  $\ln F$  in Hz. Doped samples show better efficiency on a wide range of frequencies. The reason behind this improvement of quality in the capacitive materials is due to addition of conductive ions. Energy dissipation prominently decreases due to addition of Ce and Zr salts into the zeolite porous matrix. Along with decrease in energy losses, capacitance capability also increases, hence resulting increase in the quality of the energy storage material.

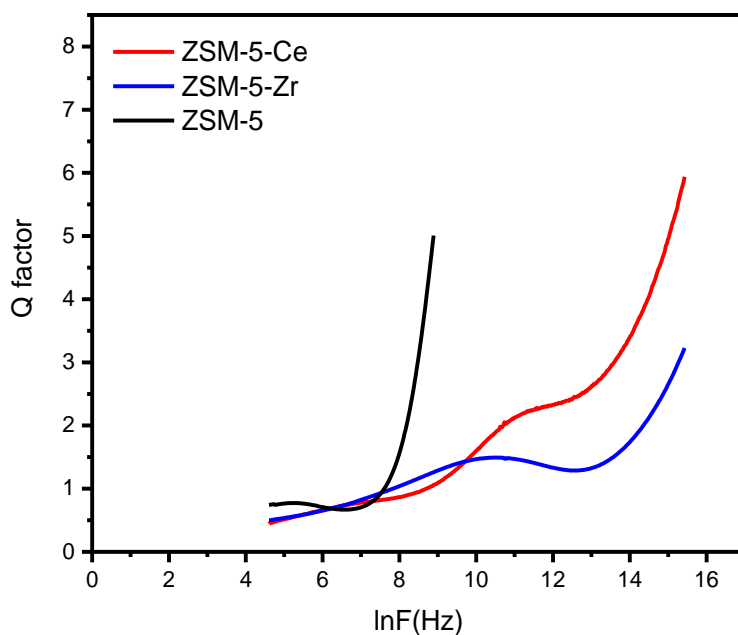


Figure 35: Plot of Q-factor vs lnF

## 4.6 Water Splitting

### 4.6.1 Onset and overpotential

Onset potential refers to the point on X axis where the current density starts rising from zero. From figure given below it can be seen that the onset potential of all the three samples lie near 1.65 volts. But if we talk about onset potential at current density of  $10\text{mAcm}^{-2}$ , it is different for all the three samples. Its nearly 1.89V for pure ZSM-5 and 1.74V for Cerium and Zirconium doped ZSM-5 zeolite.

Overpotential refers to the extra potential required over the equilibrium potential to reach the current density of  $10\text{mAcm}^{-2}$ . It is calculated by subtracting the equilibrium potential i.e. 1.23V for a normal water splitting reaction, from the onset potential of the catalyst and then multiplying it with 1000 to get overpotential in millivolts.

According to figure shown below, the over potential of pure ZSM-5 is about 660 mV and that of doped zeolites is 510 mV of both samples. Which is much greater than reported overpotentials of catalysts for water splitting. Reason behind this large overpotential is the ceramic matrix. In pure ZSM-5 there exists least number of electrons and other mobile conducting ions, which are bound in the zeolite matrix, so a high amount of electrical energy

is required to displace them, so that they can take part in water splitting. When a dopant specie is added into matrix, the threshold potential remains the same but when such voltage reaches, it supports water splitting enormously, resulting in high potential voltages obtained.

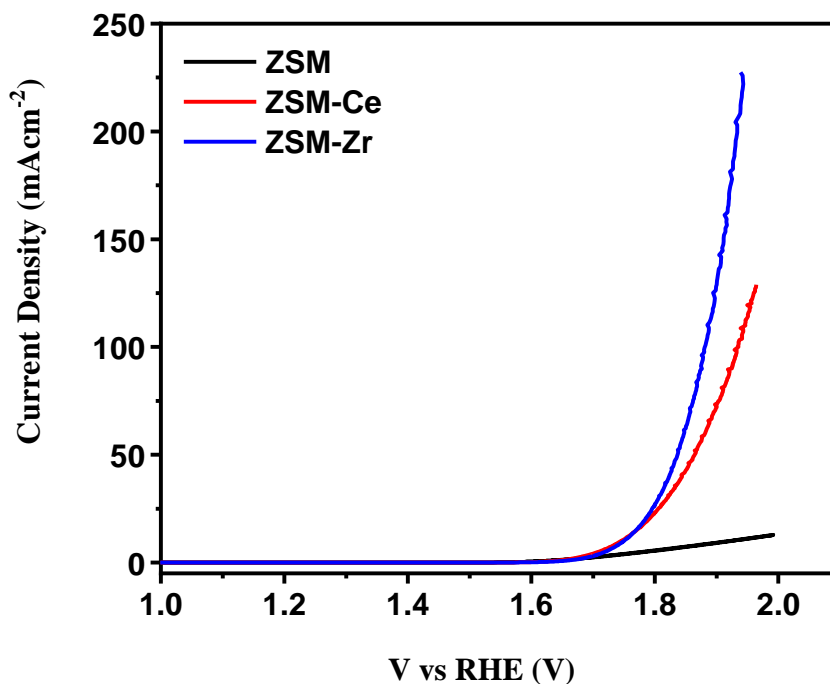


Figure 36: Current generation potential vs current density

#### 4.6.2 Tafel slope

It is the best parameter which tells us about the activity of a catalyst related to any particular reaction, either it is HER or OER. It uses logarithmic values to tell us the increase or decrease in potential per decade of catalyst. According to this parameter, the least steeper is the slope, better is the catalyst. Best reported Tafel slope results have been obtained by Ni-Fe oxides upon Platinum matrix, but due to cost effectiveness, it is not economical on a larger scale. Without platinum matrix, these Ni-Fe oxides show slope at 120-210 approx.

According to the results shown in the figure, Zr doped ZSM-5 shows the best OER kinetics as compared to other two samples and pure ZSM-5 shows the worst activity. Because the least steep slope is of Zr-ZSM-5 and most steep slope is shown by ZSM-5 sample. Zr-ZSM-5 shows best Tafel slope of the three samples. And Ce-ZSM-5 shows much better slope as compared to ZSM-5 showing Tafel slope of 355mV/dec.

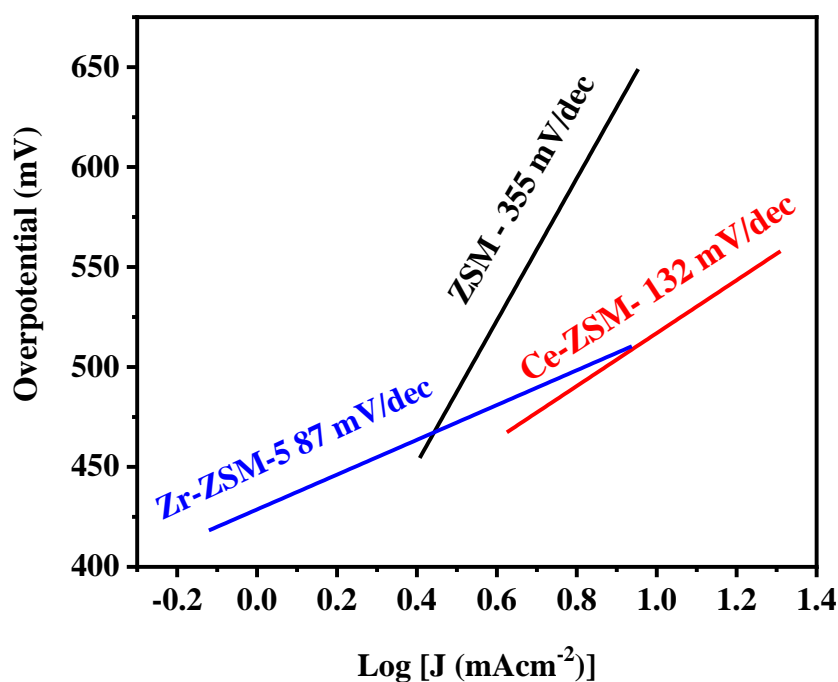


Figure 37: Tafel slope analysis

### 4.6.3 Nyquist plot

It refers to the study of resistance offered by a catalyst and the whole system during the whole process of water splitting. It accounts for the resistance offered by catalyst represented as  $R_{ac}$  and resistance offered by the electrolytic solution. It also depends upon the shape of the plot because normally a Nyquist plot shows a curve touching the x-axis twice. And the difference between these two points accounts for the resistance offered by catalyst and the initial part shows resistance offered by the electrolyte.

According to the results shown in the figure, for ZSM-Zr sample, the resistance offered by the electrolytic solution and system is about 7 ohms and that offered by catalyst was 21 ohms. The less resistance offered as compared to pure matrix is due to increase in number of conducting ions in the matrix due to doping with transition element salts.

For the rest two samples, the graph line does not reach the x-axis completely, so to obtain results from these plots we would have to extra plot these results.

By extra-plotting these results we come to know that resistance offered by Ce doped sample is approximately 30 ohms and that by pure ZSM-5 sample it would be 40 ohms. Such resistance is offered by porous matrix of zeolite. Ceramic materials, despite containing conducting ions,

offer enough resistance due to difficulty in movement of ions. Cerium sample despite having more electrons in valence shell as compared to Zr sample, shows higher resistance, this may appear due to vibration of valence shell electrons, caused by current generated during water splitting.

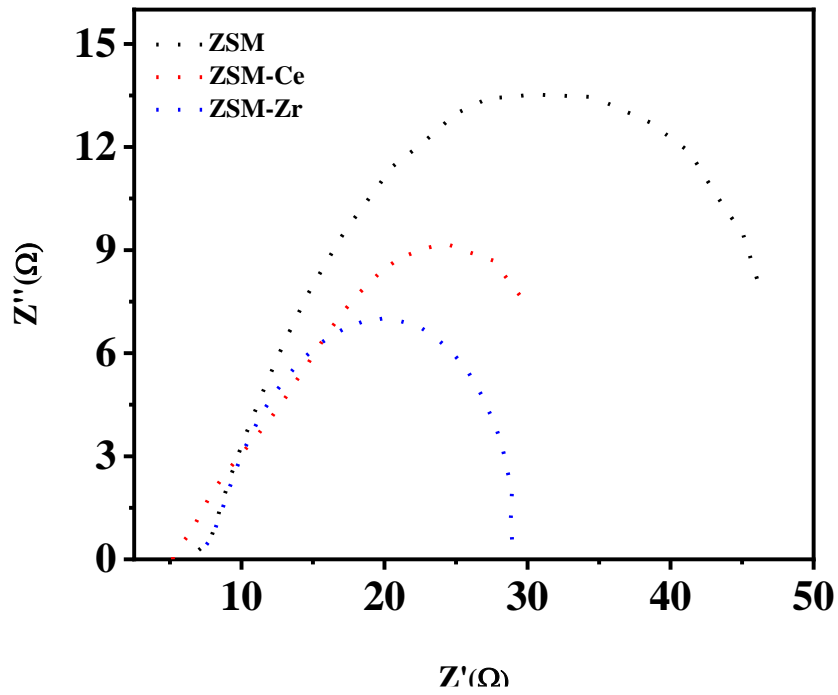


Figure 38: Nyquist plots

# Conclusions

ZSM-5 zeolite was synthesized in a greener way by using no solvent during synthesis. Two intrinsically doped samples of same zeolite were prepared by same procedure having ratio 1:4 by mass. During the study of their electrochemical properties, it was observed that doping with transition metal salts caused a huge positive change in their activities. Ce doped ZSM-5 was found showing  $7.5 \times 10^3$  F/m dielectric constant with tan loss of 2.2. They were found to be electrochemically active materials for dielectric capacitance purposes and somehow for water splitting. Zr doped ZSM-5 showed tafel slope of 87 mV/dec, which is much better than reported oxygen evolution catalysts.



---

## Chapter 5 - References

---

1. U.N. Foundation, *Sustainable Energy for All*.
2. IEO, *International energy outlook 2016*. 2016.
3. Conti, J.J., et al., *Annual energy outlook 2014*. US Energy Information Administration, 2014. **2**.
4. Van de Krol, R. and M. Grätzel, *Photoelectrochemical hydrogen production*. Vol. 90. 2012: Springer.
5. Sweeney, C., et al., *Seasonal climatology of CO<sub>2</sub> across North America from aircraft measurements in the NOAA/ESRL Global Greenhouse Gas Reference Network*. Journal of Geophysical Research: Atmospheres, 2015. **120**(10): p. 5155-5190.
6. Carmichael, P., *Materials and Devices for Photoelectrochemical and Photocatalytic Water Splitting*. 2016, UCL (University College London).
7. McGlade, C. and P. Ekins, *The geographical distribution of fossil fuels unused when limiting global warming to 2 C*. Nature, 2015. **517**(7533): p. 187-190.
8. Cammack, R., M. Frey, and R. Robson, *Hydrogen as a fuel: learning from nature*. 2001: CRC Press.
9. Singh, S., et al., *Hydrogen: A sustainable fuel for future of the transport sector*. Renewable and Sustainable Energy Reviews, 2015. **51**: p. 623-633.
10. Commission, E., *Electricity generated from renewable energy sources*. EU, 2004. **28**.
11. UK, G.o., *UK National Reform Program 2017*. 2017.
12. Lewis, N.S., *Powering the planet*. MRS bulletin, 2007. **32**(10): p. 808-820.
13. Barbose, G., N. Darghouth, and R. Wiser, *Tracking the Sun V: An historical summary of the installed price of photovoltaics in the United States from 1998 to 2011*. 2012, Lawrence Berkeley National Lab.(LBNL), Berkeley, CA (United States).
14. .
15. Lewis, N.S. and D.G. Nocera, *Powering the planet: Chemical challenges in solar energy utilization*. Proceedings of the National Academy of Sciences, 2006. **103**(43): p. 15729-15735.
16. Holladay, J.D., et al., *An overview of hydrogen production technologies*. Catalysis today, 2009. **139**(4): p. 244-260.
17. Lee, T., S.H. Ko, and R. Ryoo. *Electrical Double Layer Capacitance of Ultra-Microporous Carbon Synthesized Using Zeolite Template*. in *ECS Meeting Abstracts*. 2018. IOP Publishing.
18. Wu, Y., et al., *Enhanced energy storage properties in sodium bismuth titanate-based ceramics for dielectric capacitor applications*. Journal of Materials Chemistry C, 2019. **7**(21): p. 6222-6230.
19. Gamayunov, N., V. Murtsovkin, and A. Dukhin, *Pair interaction of particles in electric field. 1. Features of hydrodynamic interaction of polarized particles*. Colloid J. USSR (Engl. Transl.);(United States), 1986. **48**(2).
20. Dukhin, A. and V. Murtsovkin, *Pair interaction of particles in electric field. 2. Influence of polarization of double layer of dielectric particles on their hydrodynamic interaction in a stationary electric field*. Colloid J. USSR (Engl. Transl.);(United States), 1986. **48**(2).
21. Williams, M.V., H.R. Kunz, and J.M. Fenton, *Analysis of polarization curves to evaluate polarization sources in hydrogen/air PEM fuel cells*. Journal of The Electrochemical Society, 2005. **152**(3): p. A635.
22. Kasap, S.O., *Principles of electronic materials and devices*. Vol. 2. 2006: McGraw-Hill New York.
23. Stern, M., *Electrochemical Polarization: III. Further Aspects of the Shape of Polarization Curves*. Journal of The Electrochemical Society, 1957. **104**(11): p. 645.

24. Stern, M. and A.L. Geary, *Electrochemical polarization: I. A theoretical analysis of the shape of polarization curves*. Journal of the electrochemical society, 1957. **104**(1): p. 56.
25. Thakur, V.K. and R.K. Gupta, *Recent progress on ferroelectric polymer-based nanocomposites for high energy density capacitors: synthesis, dielectric properties, and future aspects*. Chemical reviews, 2016. **116**(7): p. 4260-4317.
26. Burn, I. and D. Smyth, *Energy storage in ceramic dielectrics*. Journal of Materials Science, 1972. **7**(3): p. 339-343.
27. Wu, S., et al., *Polar-fluoropolymer blends with tailored nanostructures for high energy density low loss capacitor applications*. Applied Physics Letters, 2011. **99**(13): p. 132901.
28. Wang, J., et al., *Recent progress in cobalt-based heterogeneous catalysts for electrochemical water splitting*. Advanced materials, 2016. **28**(2): p. 215-230.
29. Roger, I., M.A. Shipman, and M.D. Symes, *Earth-abundant catalysts for electrochemical and photoelectrochemical water splitting*. Nature Reviews Chemistry, 2017. **1**(1): p. 1-13.
30. Walter, M.G., et al., *Solar water splitting cells*. Chemical reviews, 2010. **110**(11): p. 6446-6473.
31. Nocera, D.G., *The artificial leaf*. Accounts of chemical research, 2012. **45**(5): p. 767-776.
32. Dresselhaus, M. and I. Thomas, *Alternative energy technologies*. Nature, 2001. **414**(6861): p. 332-337.
33. Gray, H., *Powering the planet with solar fuel*. Nat Chem **1**: 7–7. 2009.
34. Lee, Y., et al., *Synthesis and activities of rutile IrO<sub>2</sub> and RuO<sub>2</sub> nanoparticles for oxygen evolution in acid and alkaline solutions*. The journal of physical chemistry letters, 2012. **3**(3): p. 399-404.
35. Kanan, M.W. and D.G. Nocera, *In situ formation of an oxygen-evolving catalyst in neutral water containing phosphate and Co<sup>2+</sup>*. Science, 2008. **321**(5892): p. 1072-1075.
36. Suntivich, J., et al., *A perovskite oxide optimized for oxygen evolution catalysis from molecular orbital principles*. Science, 2011. **334**(6061): p. 1383-1385.
37. Gong, M., et al., *An advanced Ni–Fe layered double hydroxide electrocatalyst for water oxidation*. Journal of the American Chemical Society, 2013. **135**(23): p. 8452-8455.
38. Cobo, S., et al., *A Janus cobalt-based catalytic material for electro-splitting of water*. Nature materials, 2012. **11**(9): p. 802-807.
39. Song, F. and X. Hu, *Exfoliation of layered double hydroxides for enhanced oxygen evolution catalysis*. Nature communications, 2014. **5**(1): p. 1-9.
40. Wang, Z.-L., et al., *C and N hybrid coordination derived Co–C–N complex as a highly efficient electrocatalyst for hydrogen evolution reaction*. Journal of the American Chemical Society, 2015. **137**(48): p. 15070-15073.
41. Hinnemann, B., et al., *Biomimetic hydrogen evolution: MoS<sub>2</sub> nanoparticles as catalyst for hydrogen evolution*. Journal of the American Chemical Society, 2005. **127**(15): p. 5308-5309.
42. McKone, J.R., et al., *Ni–Mo nanopowders for efficient electrochemical hydrogen evolution*. ACS catalysis, 2013. **3**(2): p. 166-169.
43. Voiry, D., et al., *Enhanced catalytic activity in strained chemically exfoliated WS<sub>2</sub> nanosheets for hydrogen evolution*. Nature materials, 2013. **12**(9): p. 850-855.
44. Kibsgaard, J., et al., *Engineering the surface structure of MoS<sub>2</sub> to preferentially expose active edge sites for electrocatalysis*. Nature materials, 2012. **11**(11): p. 963-969.
45. Wang, H., et al., *Electrochemical tuning of vertically aligned MoS<sub>2</sub> nanofilms and its application in improving hydrogen evolution reaction*. Proceedings of the National Academy of Sciences, 2013. **110**(49): p. 19701-19706.
46. Popczun, E.J., et al., *Nanostructured nickel phosphide as an electrocatalyst for the hydrogen evolution reaction*. Journal of the American Chemical Society, 2013. **135**(25): p. 9267-9270.

47. Liu, Q., et al., *Carbon nanotubes decorated with CoP nanocrystals: a highly active non-noble-metal nanohybrid electrocatalyst for hydrogen evolution*. *Angewandte Chemie International Edition*, 2014. **53**(26): p. 6710-6714.
48. Popczun, E.J., et al., *Highly active electrocatalysis of the hydrogen evolution reaction by cobalt phosphide nanoparticles*. *Angewandte Chemie*, 2014. **126**(21): p. 5531-5534.
49. Roger Barba, I., *Investigations into electrochemical water splitting*. 2017, University of Glasgow.
50. Du, P. and R. Eisenberg, *Catalysts made of earth-abundant elements (Co, Ni, Fe) for water splitting: recent progress and future challenges*. *Energy & Environmental Science*, 2012. **5**(3): p. 6012-6021.
51. designs, I.P.
52. Tachibana, Y., L. Vayssieres, and J.R. Durrant, *Artificial photosynthesis for solar water-splitting*. *Nature Photonics*, 2012. **6**(8): p. 511.
53. Formal, F.L., et al., *Challenges towards economic fuel generation from renewable electricity: the need for efficient electro-catalysis*. *CHIMIA International Journal for Chemistry*, 2015. **69**(12): p. 789-798.
54. Joya, K.S., et al., *Water-splitting catalysis and solar fuel devices: artificial leaves on the move*. *Angewandte Chemie International Edition*, 2013. **52**(40): p. 10426-10437.
55. McCrory, C.C., et al., *Benchmarking hydrogen evolving reaction and oxygen evolving reaction electrocatalysts for solar water splitting devices*. *Journal of the American Chemical Society*, 2015. **137**(13): p. 4347-4357.
56. Faber, M.S. and S. Jin, *Earth-abundant inorganic electrocatalysts and their nanostructures for energy conversion applications*. *Energy & Environmental Science*, 2014. **7**(11): p. 3519-3542.
57. Nocera, D., *Accounts of Chem.* 2012, Res.
58. Grigoriev, S., V. Poremsky, and V. Fateev, *Pure hydrogen production by PEM electrolysis for hydrogen energy*. *International Journal of Hydrogen Energy*, 2006. **31**(2): p. 171-175.
59. Barbir, F., *PEM electrolysis for production of hydrogen from renewable energy sources*. *Solar energy*, 2005. **78**(5): p. 661-669.
60. Ayers, K.E., et al., *Research advances towards low cost, high efficiency PEM electrolysis*. *ECS transactions*, 2010. **33**(1): p. 3.
61. Dincă, M., Y. Surendranath, and D.G. Nocera, *Nickel-borate oxygen-evolving catalyst that functions under benign conditions*. *Proceedings of the National Academy of Sciences*, 2010. **107**(23): p. 10337-10341.
62. IEO, *International Energy Outlook*. 2016.
63. Lundberg, M., *Model calculations on some feasible two-step water splitting processes*. *International journal of hydrogen energy*, 1993. **18**(5): p. 369-376.
64. Zhuang, H.L. and R.G. Hennig, *Single-layer group-III monochalcogenide photocatalysts for water splitting*. *Chemistry of Materials*, 2013. **25**(15): p. 3232-3238.
65. Najafi, L., et al., *Carbon nanotube-supported MoSe<sub>2</sub> holey flake: Mo<sub>2</sub>C ball hybrids for bifunctional pH-universal water splitting*. *ACS nano*, 2019. **13**(3): p. 3162-3176.
66. Joy, J., J. Mathew, and S.C. George, *Nanomaterials for photoelectrochemical water splitting—review*. *International Journal of hydrogen energy*, 2018. **43**(10): p. 4804-4817.
67. Sasaki, Y., et al., *Solar water splitting using powdered photocatalysts driven by Z-schematic interparticle electron transfer without an electron mediator*. *The Journal of Physical Chemistry C*, 2009. **113**(40): p. 17536-17542.
68. Guidelli, R., et al., *Defining the transfer coefficient in electrochemistry: An assessment (IUPAC Technical Report)*. *Pure and Applied Chemistry*, 2014. **86**(2): p. 245-258.
69. Davis, M.E., *Zeolites and molecular sieves: not just ordinary catalysts*. *Industrial & Engineering Chemistry Research*, 1991. **30**(8): p. 1675-1683.

70. Hartmann, M., *Hierarchical zeolites: a proven strategy to combine shape selectivity with efficient mass transport*. *Angewandte Chemie International Edition*, 2004. **43**(44): p. 5880-5882.
71. Caruso, F., R.A. Caruso, and H. Möhwald, *Nanoengineering of inorganic and hybrid hollow spheres by colloidal templating*. *Science*, 1998. **282**(5391): p. 1111-1114.
72. Wang, X., et al., *Investigating the role of zeolite nanocrystal seeds in the synthesis of mesoporous catalysts with zeolite wall structure*. *Chemistry of Materials*, 2011. **23**(20): p. 4469-4479.
73. Dai, C., et al., *Synthesis of hollow nanocubes and macroporous monoliths of silicalite-1 by alkaline treatment*. *Chemistry of Materials*, 2013. **25**(21): p. 4197-4205.
74. Zuo, Y., et al., *Modification of small-crystal titanium silicalite-1 with organic bases: Recrystallization and catalytic properties in the hydroxylation of phenol*. *Applied Catalysis A: General*, 2013. **453**: p. 272-279.
75. Vermeiren, W. and J.-P. Gilson, *Impact of zeolites on the petroleum and petrochemical industry*. *Topics in Catalysis*, 2009. **52**(9): p. 1131-1161.
76. Perego, C. and A. Carati, *14 Zeolites and zeolite-like materials in industrial catalysis*. 2008.
77. Naber, J., et al., *Industrial applications of zeolite catalysis*, in *Studies in surface science and catalysis*. 1994, Elsevier. p. 2197-2219.
78. Feng, H., C. Li, and H. Shan, *In-situ synthesis and catalytic activity of ZSM-5 zeolite*. *Applied clay science*, 2009. **42**(3-4): p. 439-445.
79. April, J., et al. *Advanced optimization methodology in the oil and gas industry: the theory of scatter search techniques with simple examples*. in *SPE Hydrocarbon Economics and Evaluation Symposium*. 2003. Society of Petroleum Engineers.
80. Agustriyanto, R. and A. Fatmawati, *Power model for enzymatic hydrolysis of coconut coir with chemical pretreatment*. 2016.
81. Dean, J., *Analytical Chemistry Hand Book* “, McGraw-Hill Inc., New York. 1995.
82. Cahn, R.W. and E. Lifshitz, *Concise encyclopedia of materials characterization*. 2016: Elsevier.
83. Heineman, W.R., P.T. Kissinger, and P. Kissinger, *Large-amplitude controlled-potential techniques*. 1996: Marcel Dekker: New York.
84. Mandler, D., *Fritz Scholz (Ed.): Electroanalytical methods. Guide to experiments and applications*. 2010, Springer.
85. Hagen, G., et al., *Selective impedance based gas sensors for hydrocarbons using ZSM-5 zeolite films with chromium (III) oxide interface*. *Sensors and Actuators B: Chemical*, 2006. **119**(2): p. 441-448.
86. Praveena, K. and S. Murthy, *Dielectric Properties of Dehydrated Zeolites*. measurements, 2013. **16**: p. 17.
87. Pervaiz, E. and I. Gul. *Influence of rare earth (Gd<sup>3+</sup>) on structural, gigahertz dielectric and magnetic studies of cobalt ferrite*. in *Journal of Physics: Conference Series*. 2013. IOP Publishing.
88. Mahabole, M., et al., *Dielectric and ethanol sensing studies on synthesized nano-ZSM-5 zeolite*. *Indian Journal of Physics*, 2015. **89**(2): p. 167-174.
89. Li, X., et al., *Nanostructured catalysts for electrochemical water splitting: current state and prospects*. *Journal of Materials Chemistry A*, 2016. **4**(31): p. 11973-12000.
90. Gashimov, A. and I. Zakieva, *Dielectric parameters of composites based on electric discharge processed natural zeolite*. *Technical Physics*, 2017. **62**(9): p. 1381-1384.
91. Anis, S.F. and R. Hashaikeh, *Electrochemical water splitting using nano-zeolite Y supported tungsten oxide electrocatalysts*. *Journal of Nanoparticle Research*, 2018. **20**(2): p. 1-11.
92. Milikić, J., et al., *NiA and NiX zeolites as bifunctional electrocatalysts for water splitting in alkaline media*. *International Journal of Hydrogen Energy*, 2018. **43**(41): p. 18977-18991.

93. Wang, J., et al., *Amorphization activated ruthenium-tellurium nanorods for efficient water splitting*. Nature communications, 2019. **10**(1): p. 1-11.
94. Lakhane, M., et al., *Dielectric properties of zeolite based metal oxide nanocomposites*. Nano-Structures & Nano-Objects, 2019. **17**: p. 248-258.
95. Pullano, S.A., et al., *An Affordable Fabrication of a Zeolite-Based Capacitor for Gas Sensing*. Sensors, 2020. **20**(7): p. 2143.
96. Abdelsayed, V., D. Shekhawat, and R.S. Tempke, *Zeolites interactions with microwaves during methane non-oxidative coupling*. Catalysis Today, 2020.
97. Zhang, H., et al., *Bifunctional heterostructured transition metal phosphides for efficient electrochemical water splitting*. Advanced Functional Materials, 2020. **30**(34): p. 2003261.
98. Wei, J., et al., *Heterostructured electrocatalysts for hydrogen evolution reaction under alkaline conditions*. Nano-micro letters, 2018. **10**(4): p. 1-15.
99. Yang, W., et al., *Electronic-structure tuning of water-splitting nanocatalysts*. Trends in Chemistry, 2019. **1**(2): p. 259-271.